Experimental study of impurity screening in the edge ergodic layer of the Large Helical Device using carbon emissions of CIII to CVI

Malay Bikas Chowdhuri*
Department of Fusion Science, Graduate University for Advanced Studies, Toki 509-5292, Gifu, Japan
Shigeru Morita, Masahiro Kobayashi and Motoshi Goto
National Institute for Fusion Science, Toki 509-5292, Gifu, Japan
Hangyu Zhou
Department of Fusion Science, Graduate University for Advanced Studies, Toki 509-5292, Gifu, Japan
Suguru Masuzaki, Tomohiro Morisaki, Kazumichi Narihara and Ichihiro Yamada
National Institute for Fusion Science, Toki 509-5292, Gifu, Japan
Yuehe Feng
Max-Planck-Institut für Plasmaphysik, Wendelsteinstrasse 1, D-17491 Greifswald, Germany

*Communicating author E-mail: chowdhuri.malay@nifs.ac.jp

Four resonance transitions of CIII (977.03Å: $2s^2\ ^1S_0$-$2s2p\ ^1P_1$), CIV (1550Å: $2s\ ^2S$-$2p\ ^2P$), CV (40.27Å: $1s^2\ ^1S_0$-$1s2p\ ^1P_1$) and CVI (33.73Å: $1s\ ^2S$-$2p\ ^2P$) have been observed in VUV and EUV regions to study the edge carbon impurity transport in the LHD ergodic layer. Here, CIII and CIV indicate the carbon influx at the outside boundary of the ergodic layer and CV and CVI indicate the ions in higher ionization stages which have already experienced the transport in the ergodic layer. The intensity ratio of CV+CVI to CIII+CIV, therefore, represents the degree of impurity screening, which has been analyzed with different edge plasma parameters and ergodic magnetic field structures. The ratio decreases by two orders of magnitude with an increase of electron density, n_e, in the range of $1–8\times10^{19}m^{-3}$. The CV and CVI emissions tend to decrease with n_e, whereas the CIII and CIV emissions monotonically increase with n_e.

The result suggests an enhancement of the impurity screening in the higher n_e range due to the increasing ion-impurity collision frequency ($\nu_{Zi} \equiv 1/\tau_s = 3.4\times10^4 s^{-1}$ at $n_e = 2\times10^{19} m^{-3}$ and $1.0\times10^5 s^{-1}$ at $6\times10^{19} m^{-3}$ for CV). The friction force parallel to the magnetic fields plays an important role in the edge impurity transport within the ergodic layer. When the ergodic layer structure is thicker, the ratio systematically decreases mainly due to a reduction of CV+CVI emissions. The ratio is also studied by changing the radial position of an externally supplied m/n=1/1 islands. When the island is positioned in the ergodic layer, the ratio indicates a remarkable change, i.e. reduction of CV+CVI and increase of CIII+CIV. These experiments demonstrate that the modification of the ergodic magnetic field structure makes a clear change to the edge impurity transport. When the background ion species is changed from hydrogen to helium, the ratio is clearly reduced, at least at $n_e \leq 4\times10^{19} m^{-3}$, suggesting the enhancement of the impurity screening effect due to the increased collisionality. Finally, the experimental result is simulated using 3-dimenstional edge transport code of EMC3-EIRENE. The density dependence of the carbon ratio can be well reproduced with a simulation code suggesting that impurity screening is induced in the ergodic magnetic field layer.

Key words: carbon, VUV emission, EUV emission, edge impurity transport, impurity screening, LHD

I. **INTRODUCTION**

Edge particle control, including the control of impurities, is one of the important issues in fusion research with relation to confinement improvement and divertor heat flux control. The impurity control becomes also important with respect to an enhancement of the bremsstrahlung emission in high-density operation, the dilution of fuel ions, and the energy loss by radiation. Active impurity control was done using an axis-symmetric poloidal divertor configuration[1], where the particle outflux is directed into a region separated from the main plasma. Another approach of the active impurity control was the stochastization of edge magnetic fields using resonant perturbations[2]. Such perturbations could ergodise the magnetic field lines by overlapping edge magnetic islands. It is reported that the enhancement of edge particle and energy transport by the stochastic magnetic fields should lead to a reduction of impurity content in the core plasma[3].

In tokamak devices, the effect of such a stochastic magnetic field structure has been generally studied using external magnetic field coils, e.g., perturbation field on DIII-D[4], the ergodic divertor (ED) on Tore Supra[5] and the dynamic ergodic divertor (DED) on TEXTOR[6]. In DIII-D, the effect of stochastization has been mainly studied to control the ELM (edge localized mode) enhanced divertor heat flux in the pedestal[7]. On the other hand, extensive studies on the impurity behavior due to ergodization of the edge magnetic fields have been carried out on Tore Supra. In Tore Supra the activation of the ED led to a significant reduction in the concentration of intrinsic impurities and to an appreciable enhancement of the radiation from the plasma edge[8]. The ED worked differently on each ionization state of highly charged impurity ions[9]. In TEXTOR, the decontamination of highly ionized carbon in the plasma core was observed during DED operation[10]. These experimental results clearly demonstrate the importance of the impurity transport in the stochastic magnetic field layer, where collisions with background particles are dominant[11].

In helical devices, such as the Large Helical Device[12] (LHD), the edge magnetic fields are intrinsically stochastic. The edge plasma is therefore characterized by the presence of a thick stochastic magnetic field layer surrounding the plasma core, so called 'ergodic layer'[13]. The properties of the ergodic layer can be changed by shifting the

magnetic axis, by varying vertical magnetic field or by deforming the plasma shape, using the quadrupole magnetic field. It is interesting to study the edge impurity behavior in LHD, which is determined by a static ergodic layer formed only by the steady superconducting magnetic coils and which is therefore entirely different from tokamaks[14].

The edge particle and impurity studies started at the beginning of LHD, when LHD was still a limiter experiment[15], and have since progressed with the development of several diagnostic tools and computer simulation codes. In this paper, the edge impurity transport has been studied using the spectral emissions from carbon, which is the primary impurity in LHD as well as other fusion devices. The relevant properties of the edge magnetic field structure in LHD are described in Section II. In Section III the experimental setup used for the present study is introduced. After a brief description of theoretical background on the edge impurity transport of the ergodic layer in Section IV, the experimental results on the carbon emissions behavior are presented with the discussion in Section V. In Section VI, finally, theoretical predictions from the EMC3-EIRENE simulation code are compared with the experimental results.

II. **LHD EDGE MAGNETIC STRUCTURE**

LHD is a superconducting device with major and average minor radii of R=3.60 and a=0.64m, respectively. The magnetic field for the confinement is produced and sustained by a pair of continuous helical coils, pairs of outer and inner vertical coils, and inner shaping coils. Toroidal and poloidal pitch numbers of the helical coils are M/ℓ=10/2, respectively. Ten pairs of local island divetor[16] (LID), normal conducting, coils are set at the top and bottom ports of all vertically elongated plasma cross sections. These LID coils are basically used for the cancellation or expansion of m/n=1/1 island. The plasma axis position, which causes remarkable changes in the structures of both the magnetic surface and the ergodic layer, can be moved horizontally by changing the vertical field by means of the outer and inner vertical coils. Schematic views of the LHD magnetic configurations at horizontally elongated cross sections of R_{ax} = 3.60 and 4.00m are shown in Figs.1 (a) and (b), respectively. The elliptical magnetic flux surfaces appear inside the last closed flux surface (LCFS). The position of LCFS in LHD is defined by

the outermost flux surface on which the deviation of the magnetic field line is less than 4mm after it has made 100 turns along the torus. The magnetic field in the ergodic layer has been computationally determined by following the field lines which started from several radial points at a fixed toroidal position. The calculation was terminated, when a field line had made 2000 toroidal turns or it had reached the divertor plates. When a field line has made 2000 toroidal turns, it has, by definition, reached the last closed flux surface. When the edge density profile is compared with the connection length, it reveals that an enough density can be formed in a region where the connection length is at least longer than 100m. The edge density profile in the ergodic layer measured by reciprocating probe agrees well with such detailed predictions of the magnetic field structure[17].

The LCFS is surrounded by the ergodic layer. The ergodic layer is naturally formed by overlapping magnetic islands with many modes depending on the radial magnetic field, which is generated by the helical coils. The volume of the ergodic layer is much larger in the case with R_{ax}=4.00m than in the case with R_{ax}=3.60m as indicated in Fig.1. The thickness of the ergodic layer varies with the poloidal angle. The thickness reaches its minimum value of 1-2cm at the O-points located near the helical coils for the case with R_{ax}=3.60m. The ergodic layer typically consists of stochastic magnetic field lines with lengths from 10 to 2000m, which correspond to 0.5-100 toroidal turns around the torus. The thickness of the ergodic layer, λ_{erg}, increases with the outward shift of the magnetic axis. It can be seen that the λ_{erg} at inboard side becomes very large for outwardly shifted plasma configurations. Ergodicity is defined by the inverse of the Kolmogorov length, L_k^{-1}. In LHD, the L_k^{-1} basically increases when the location moves outboard along the major radius. When the ergodic layer becomes thicker, the L_k^{-1} becomes larger at the periphery of the ergodic layer, so that the ergodicity in a thick ergodic layer is always large[18]. Outside of the ergodic layer, there exist four intrinsic divertor legs between the X-points and divertor plates. The particle flux out of the plasma core reaches the divertor plates through the ergodic layer via the divertor legs.

Edge profiles of the magnetic field connection length, L_c, are illustrated in Figs.2 (a) and (b) at the horizontally elongated plasma cross sections for R_{ax}=3.60 and 4.00m, respectively. The LCFS position is shown by a solid vertical line and typical range of the

ergodic layer is indicated by a thick horizontal bar. As one can see, the ergodic layer consists of field lines with short and long connection lengths. The long field lines work as the main channel of the particle and heat outfluxes. The number of field lines with a short connection length of $L_c \leq 100$m increases towards the periphery of the ergodic layer, which is known as the edge surface layer. Long connection lengths also appear in the edge surface layer within a narrow, discrete region and coexist together with short connection lengths. This structure is a unique feature of the LHD intrinsic divertor configuration. The short field lines provide particle and energy sinks for the long field lines via perpendicular transport.

III. **EXPERIMENTAL SETUP**

An LHD discharge is generally initiated by electron cyclotron heating (ECH) and then sustained and heated by the injection of three negative-ion-based neutral beams (NBI). The maximum total heating power of the NBIs is 18MW. The electron density and electron temperature in LHD discharges with gas puff are typically $n_e \leq 10^{20}m^{-3}$ and $T_e \leq 3$keV. Operation at higher densities up to $10^{21}m^{-3}$ is possible using H_2 pellet injection. Carbon emissions have been monitored using resonance transitions of CIII (977Å, $2s^2\ ^1S$-$2s2p\ ^1P$), CIV (1548Å, $2s\ ^2S$-$2p\ ^2P$), CV (40.27Å, $1s^2\ ^1S$-$1s2p\ ^1P$) and CVI (33.73Å, $1s\ ^2S$-$2p\ ^2P$). The CIII and CIV lines, in VUV range, are observed using two absolutely calibrated 20cm normal incidence vacuum ultraviolet (VUV) monochromators equipped with secondary electron multiplier (SEM) tube detectors[19]. The signal is usually acquired within a time interval of 100μs. An absolute intensity calibration is obtained by measuring the intensity ratio of 3p-2s transition and the 2p-2s transition and applying the branching ratio method where the carbon emissions are measured by an absolutely calibrated flat-field extreme ultraviolet (EUV) spectrometer (EUV_Long: 50–500Å range)[20]. The spectral lines from CV and CVI are observed using another absolutely calibrated flat-field EUV spectrometer[21] (EUV_Short: 10–130Å range) with a spectral resolution of ~0.10Å at 40Å. Back-illuminated VUV sensitive charge-coupled device (CCD) detectors are mounted on both spectrometers and operated in full-binning mode, where all the vertical pixel signals are summed up in a single bottom pixel and makes a

simple function as a linear detector. The CCD detectors are cooled down to -20°C using Peltier devices in usually used operational condition. Data from the CCD are acquired in every 5ms with good signal-to-noise ratio.

Vertical profiles of CIII (4650Å), CIV (5810Å) and CV (2271Å) emissions have been observed using a visible spectrometer for the Z_{eff} profile measurement[22]. The system consists of an astigmatism-corrected Czerny-Turner-type spectrometer with a CCD camera for visible light and a vertical array of 44 optical fibers. The 30cm focal length spectrometer is equipped with a toroidal, a flat and two spherical mirrors and three gratings (110, 120, and 1200 grooves/mm) and covers the wavelength range of 2000–9000Å. The optical fiber (core diameter: 100μm) in combination with a lens (focal length: 30mm) provide a spatial resolution of 30mm at the plasma center. Electron temperature and density profiles are measured with the Thomson scattering diagnostics. Line-integrated electron density is measured with the Far InfraRed (FIR) diagnostics. The ion saturation current measured by Langmuir probes, embedded in the divertor plates, is used in the present study as a density monitor at the divertor.

IV. BRIEF DESCRIPTION ON IMPURITY TRANSPORT IN ERGODIC LAYER

Analysis of impurity transport in the ergodic magnetic field layer of LHD, with a troidally non uniform magnetic structure should be done with a three-dimensional treatment of the magnetic field lines, as mentioned in section VI. For a better understanding of the physical background on the edge impurity transport we describe here the usually used formulation of a simple 1D model for the transport parallel and perpendicular to the field lines.

In the fluid description, the impurity transport along the field lines is governed by the momentum equation;

$$\mathbf{m_z}\frac{\partial \mathbf{V_{z\|}}}{\partial \mathbf{t}} = -\frac{\mathbf{1}}{\mathbf{n_z}}\frac{\partial \mathbf{T_i n_z}}{\partial \mathbf{s}} + \mathbf{m_z}\frac{\mathbf{V_{i\|}} - \mathbf{V_{z\|}}}{\boldsymbol{\tau}_{\mathbf{zi}}} + \mathbf{ZeE_{\|}} + \mathbf{0.76Z^2}\frac{\partial \mathbf{T_e}}{\partial \mathbf{s}} + \mathbf{2.6Z^2}\frac{\partial \mathbf{T_i}}{\partial \mathbf{s}} \quad , \qquad (1)$$

where the subscript of z and i denote the impurity ion with a charge state Z and the background ion, respectively. The parameter of s is the coordinate along the field line. The symbols of τ_{zi}, $E_{||}$ and $V_{||}$ denote the impurity-ion collision time, the parallel electric

field and the parallel flow velocity, respectively. It is assumed that the ion temperature of impurity, T_z, is equal to the ion temperature of the background ion, T_i. The first term on the right hand side is the force due to the impurity pressure gradient (FPG). The second and third terms are the force due to friction (FF) between impurity and background ions and the force due to parallel electric field (FE), respectively. The FF drives the impurity ion towards the divertor (downstream) and the FE pushes the impurity ions along the electric field. The fourth and fifth terms on the right hand side are the forces due to electron (FeG) and ion (FiG) temperature gradients, respectively. Both of them drive the impurity ions towards the high temperature region (upstream). Among these terms, the FF and FiG terms are dominant for our usual plasma parameters[23]. For the typical edge plasma parameters in LHD of T_e=100eV, T_i=150eV, $n_i=10^{19}m^{-3}$, and L_c=50m for He-like CV (C^{+4}) ions, the values of the force terms mentioned above, are

$$\mathbf{FF} \sim m_z \times 0.5 c_s / \tau_{CV,i} = 1.3 \times 10^{-17},$$
$$\mathbf{FE} \sim z \times T_e / L_c = 1.3 \times 10^{-18},$$
$$\mathbf{FiG} \sim 2.6 Z^2 \times T_i / L_c = 2.0 \times 10^{-17} \text{ and}$$
$$\mathbf{FeG} \sim 0.71 Z^2 \times T_e / L_c = 3.0 \times 10^{-18} \text{ kg.m.s}^{-2},$$

where $\tau_{CV,i}$ ~1.16×10^{-4}s. The relations of FF>FE and FiG>FeG are valid under these conditions. The FPG term becomes very weak, since the parallel density gradient is relatively small. The force balance between FF and FIG, i.e., friction force and thermal force, thus defines the direction of the impurity flow. The impurity velocity along field lines is expressed by

$$V_{z\|} = V_{i\|} + 2.6 Z^2 \frac{\tau_{zi}}{m_z} \frac{\partial T_i}{\partial s}. \quad (2)$$

The flow, characterized by $V_{i\|}$, is downstream and the flow, driven by the gradient of $\partial T_i / \partial s$, is upstream. The impurity flow is downstream, when the thermal force is dominated by the friction force. The ratio between these two forces[24] can be written as

$$\frac{\text{friction force}}{\text{thermal force}} \sim \frac{2.5 n_i T_i V_{i\|}}{\kappa_i^0 T_i^{2.5} \nabla_\| T_i} \propto \frac{n_i |M|}{T_i \nabla_\| T_i}, \quad (3)$$

where M is the Mach number and κ_i^0 the parallel heat transport coefficient. The numerator and denominator represent convective and conductive energy fluxes, respectively.

The radial transport in the ergodic layer is described by the 1D radial continuity equation for the impurity flux[24]

$$\frac{\partial}{\partial r}\left(\Theta\, n_I V_{z\|} - D_I \frac{\partial n_I}{\partial r}\right) = 0, \tag{4}$$

since the source term can be neglected because of the short ionization mean free path of neutral impurity. Here, the symbol of r defines the radial direction in the plasma, and n_I is the impurity density summed over all charge states. The value of D_I expresses the cross field diffusion coefficient for the impurities. The symbol Θ denotes the field line pitch inside the remnant islands in the ergodic layer, which is defined as dr/dl with dl being the parallel path along island separatrix for a radial displacement of dr. The equation can be integrated and replaced by[25]

$$n_I(r) = n_I(a)\exp\left(-\int_r^a \frac{\Theta V_{z\|}}{D_I} dr\right), \tag{5}$$

where a is the position of the outermost boundary of the ergodic layer. The equation indicates that the impurity is screened in the ergodic layer, if the velocity of the outward impurity flow, $V_{z\|}>0$. In the following discussion it is assumed that the perpendicular transport coefficients do not change much even if the edge parameters such as the density and magnetic field line structure change considerably.

V. EXPERIMENTAL RESULTS AND DISCUSSIONS

The fractional abundance of the carbon ions at the plasma center is calculated using the 1-d transport code[26] assuming a diffusion coefficient of $D=0.1 m^2/s$, which is used to study the core transport properties of LHD plasmas[27]. Figure 3 shows the fractional abundance of carbon ions. Since the abundance of carbon ions, located at plasma edge, are also a function of the convection velocity, the radial position of each carbon ion should shift toward the region with higher temperature. However, the figure is still useful for an understanding of the ionization balance of carbon. The Be-like (CIII)

and Li-like (CIV) ions are located in a very low temperature region of T_e<15eV. The He-like (CV) and H-like (CVI) ions, on the other hand, are located in a region, 15<T_e<200eV, which is clearly separated from the region of CIII and CIV. This is a very important fact in the present study. Since the edge temperatures at the LCFS (ρ=1) in LHD are usually in a range of 50≤T_e≤500eV, except for the extremely high-density range, the CIII and CIV ions always exist on the outer side of the ergodic layer, whereas the CV and CVI ions exist near the LCFS (see typical edge T_e profiles, e.g., Fig.7).

The radial profiles of the impurities have been observed using a visible spectrometer for bremsstrahlung profile measurement. Typical examples of the vertical profiles of the CIII, CIV and CV emissions measured at R_{ax}=3.6m are shown in Fig.4. The magnetic field configuration for the case of R_{ax}=3.6m is traced in Fig.5 for a poloidal cross section along the viewing angle of the visible spectrometer. Here, we point out that a few viewing chords at the bottom side, near Z= -0.4m, are blocked by the rid of the vacuum vessel. The CIII and CIV profiles in Fig.4 indicate a remarkable non uniformity reflecting the field line structure of the ergodic layer. The peaks of the CIII and CIV profiles seen in the same vertical location of Z=0.46m indicate that the edge emission is usually observed from upper side ('+' means upper side and '-' means lower side in Fig.5) of the LHD elliptical plasma at the horizontally elongated plasma cross section. The edge emission can be enhanced by the long chord length along the plasma edge at the top side, as seen in Fig.5. Whereas both peaks at Z=0.37m for CIII and at Z=0.09m for CIV originate from emissions in the ergodic layer near the inboard side X-point. The field lines near the inboard side X-point are directly connecting to divertor plates. Since the field line structure is complicated due to its chaotic nature, which results in a specific particle behavior in the three-dimensional space, the transport has not been fully understood at present. However, it can be argued that the electron temperature and density are not uniform along the poloidal angle in the ergodic layer and that the location of impurity ions in each ionization stage can be determined by the non uniform temperature and density structures, so that the CIV peak is not observed at the same position as CIII. Such an inhomogeneous poloidal distribution was, for instance, also observed in neutral hydrogen and helium emissions by a 2-dimensional profile measurement, using Zeeman spectroscopy[28]. These inhomogeneous poloidal distributions

mainly arise from inhomogeneities in the neutral particle density[29]. This is the reason why such non uniform profiles are seen in the CIII and CIV. However, the CV profile does not express any strong asymmetric character, which strongly suggests that the CV ion distribution is only a function of the magnetic surface. The CV intensity gradually increases when the line-of-sight is moved from the bottom to the top of the elliptical plasma. This continuous change in intensity originates mainly from the different chord integration lengths in the edge plasma.

Spectral emissions from CIII, CIV, CV and CVI have been analyzed during the steady state phase of several NBI discharges in LHD. Since the ionization energies of CIII (48eV) and CIV (64eV) are very small compare to the CV (392eV) and CVI (490eV), there exists a clear separation of the carbon ions in these different four ionization stages in the radial direction, as mentioned before. The four charge states of carbon ions can thus be divided into two groups, i.e., CIII+CIV and CV+CVI. The CIII and CIV, existing at outer side in the ergodic layer, can be taken as the source term representing the influx of carbon, while the CV and CVI existing near the LCFS can be taken as the ions, which have already experienced the transport through the ergodic layer. The intensity ratio of the two groups can, therefore, be considered as a measure for the degree of the impurity screening. This ratio was analyzed to study the edge impurity transport for different edge plasma parameters and ergodic magnetic field structures.

A. DENSITY DEPENDENCE OF CARBON EMISSIONS

The ratio of CV+CVI to CIII+CIV as a function of line-averaged electron density, $\langle n_e \rangle$, is plotted in Fig.6 (a). The ratios drop by two orders in magnitude when the density rises from 1 to $8\times10^{19}m^{-3}$. This drop is mainly due to the fact that the CIII+CIV intensity monotonically increases with n_e whereas the CV+CVI intensity tends to decrease with increasing n_e. This is also seen in the Fig.6 (b), where the CV+CVI and CIII+CIV intensities normalized to the density are plotted versus $\langle n_e \rangle$. The edge n_e and T_e profiles are plotted in Fig.7 as a function of major radius for low-density (closed circles: $\langle n_e \rangle=1.5\times10^{19}m^{-3}$) and high-density (open triangles: $5.5\times10^{19}m^{-3}$) discharges. It is clearly seen that the edge T_e is lower at higher edge n_e. During the steady state phase of

LHD discharges, the CIII and CIV intensities, normalized to the density, reflect the influx of carbon, since the excitation rate coefficients become proportional to the ionization rate coefficients. The edge T_e profile generally does not change much in LHD, when the density changes, so that, the emission volume of CV and CVI also does not change, even though the radial location changes according to the change of edge T_e. A small jump is seen in the edge n_e profiles at R=4.6m. This edge density jump is observed by the Thomson scattering diagnostics in most discharges. The reason is presently unclear. As indicated in Fig.6 (a), the drop of the intensity ratio suggests the impurity screening in the range of higher n_e. The ion-impurity collision frequency, ν_{zi}, for He-like CV ion is given by[23]

$$\nu_{zi} \equiv 1/\tau_s = \frac{\left(1 + m_i/m_z\right) z^2 n_i \ln\Lambda}{1.47\times10^{13} m_z T_i \left(T_i/m_i\right)^{0.5}} \ . \tag{6}$$

Assuming T_i=100eV, the frequencies become 3.42×10^4 and $1.02\times10^5 s^{-1}$ at densities of $n_i=2\times10^{19}$ and $6\times10^{19}m^{-3}$, respectively. The increase of the collision frequency means that the contribution of the friction force is enhanced at higher densities. The friction force overcomes the thermal force in the range of higher n_e, as suggested in Eq.3 and leads to the enhancement of impurity screening. This conclusion is also supported by edge particle transport EMC3-EIRENE code simulations, which are discussed in section VI.

B. CARBON EMISSIONS WITH DIFFERENT MAGNETIC AXES

When the magnetic axis is shifted, the thickness of the ergodic layer changes remarkably. Figure 8 (a) illustrates the ratio of the CV+CVI to CIII+CIV emission as a function of $<n_e>$. The ratios decrease with increasing $<n_e>$ for all magnetic axis configurations. In addition, the ratios become lower when R_{ax} is shifted outwardly. This tendency is very clear especially for densities of $\leq5\times10^{19}m^{-3}$. This reduction is mainly caused by the decrease in the CV+CVI intensity as shown in Fig.8 (b). On the contrary, the CIII+CIV intensities do not change with $<n_e>$ for all configurations, as revealed in Fig.8 (c), although the edge T_e and n_e are considerably changed by a shift of R_{ax}. This indicates that the carbon source term is nearly similar for all magnetic axes, except for

R_{ax}=3.60m, where the source term is somewhat different at the low densities. The reduction of the CV+CVI, therefore, suggests an enhancement of the impurity screening for increasing values of R_{ax}. The small increase in the ratios and intensities of CV+CVI at n_e above $6\times10^{19}m^{-3}$ for R_{ax} = 4.0m seem to originate from low energy confinement and a low NBI power deposition in the R_{ax}=4.0m configuration. In other words, shifting R_{ax} outside from R_{ax}=3.6m, the energy confinement becomes worse due to a decrease of the plasma volume, and the NBI power deposition becomes also worse due to the increased effective magnetic ripple and deviation of NBI beam center from the plasma axis. Therefore, the size of the plasma varies as the density is increased, especially in the case of R_{ax}=4.0m, due to the large reduction of the edge temperature. The thickness of the ergodic layer also changes as a function of density. The slight increase in the ratio of the CV+CVI to CIII+CIV and the intensity of CV+CVI may reflect such a dynamic change of the ergodic layer thickness in the high-density range. The structures of the ergodic layer are shown in Fig.9 for R_{ax}=3.6-4.0m. The thickness of the ergodic layer increases with an outward shift of the magnetic axis. The size of the ergodic layer plays an important role for the edge particle transport. An exact determination of the size of the ergodic layer is difficult at present because the magnetic field lines continuously expand into the outer area with a limited connection length. However, it is known from the experiments that the edge density is determined by field lines with a connection length of L_c>10m, so that, the area of the ergodic layer can practically be derived from these experimental results, as indicated by the horizontal bar in Fig.9. The thickness of the ergodic layer is plotted in Fig.10 as a function of R_{ax}. The thinnest ergodic layer is obtained for the R_{ax}=3.6m configuration, so called 'standard configuration', where LHD plasmas have the maximum volume of $30m^3$. The thickness of the ergodic layer in cases with R_{ax}=4.0 and 4.1m is 3-5 times larger than in the case with R_{ax}=3.6m, resulting in a smaller plasma volume.

Figure 11 shows the edge profiles of n_e and T_e for R_{ax}=3.6 and 4.0m. The edge density tends to have a flatter profile with increasing R_{ax} for the same line-averaged electron density. This tendency is clearly seen in Fig.11 (a). The thicker ergodic layer for R_{ax}=4.0m supports a flatter density profile with a high density compared to R_{ax}=3.6m case. The edge T_e profiles in the ergodic layer are almost similar in both cases, as shown

in Fig.11 (b), while the core T_e profiles inside the LCFS are quite different. The edge density in the ergodic layer normalized to the core density, increases with increasing ergodic layer thickness. As a result, the friction force dominates over the ion thermal force in the thick ergodic layer, so that the degree of the impurity screening becomes a function of the size of the ergodic layer. Finally, it should be mentioned that in the R_{ax}=4.0m configuration the plasma performance is worse, even though impurity ions can be well screened.

C. CARBON EMISSIONS WITH EXTERNALLY SUPPLIED m/n=1/1 MAGNETIC ISLAND

In LHD, the m/n=1/1 magnetic island can be superimposed in the edge region by means of the LID coils, where m and n are the poloidal and toroidal mode numbers, respectively. The position of the island varies with the magnetic axis, since the rotational transform changes appreciably with R_{ax}. Figure 12 shows the profiles of the rotational transform as a function of normalized radius ρ. The rotational transform profiles become gradually flatter with increasing R_{ax}. As a result, the radial location of the $\iota/2\pi$=1 surface moves to the outside region of the plasma when the R_{ax} is shifted outwardly. The position of $\iota/2\pi$=1 is located at ρ=0.83 for the R_{ax}=3.60m configuration, whereas it is inside the ergodic layer for the R_{ax}=4.00m configuration. Therefore, the m/n=1/1 island can be placed just inside the LCFS for R_{ax}=3.75m and just outside the LCFS (inside the ergodic layer) for R_{ax}=3.85m. In both cases, current was supplied to the LID coils to expand the m/n=1/1 island. The edge magnetic field structures are calculated and Poincare plots are shown in Fig.13 for horizontally elongated plasma cross section. Vertical solid lines indicate the LCFS position. The size of intrinsic m/n=1/1 island is basically small (see Fig.13 (a)). When current is supplied to the LID coils, the formation of a large island is clearly visible at outboard side of the elliptical plasma. By contrast, the formation of an island is not visible in Fig.13 (d), essentially because of the absence of a resonant field in the ergodic layer. However, depending on the current supply to the LID coils, a certain effect can be seen in the figure, which suggests that the edge impurity transport can be modified by changing the position of the m/n=1/1 island.

The line emissions from carbon were observed in both cases, i.e. during the absence and presence of the superimposed m/n=1/1 island, for R_{ax}=3.75 and 3.85m as mentioned above. The ratios of CV+CVI and CIII+CIV are plotted together with their normalized intensities as a function of $<n_e>$ in Fig.14. In the R_{ax}=3.75m configuration, the ratios do not entirely change in the cases with and without an m/n=1/1 island. However, the ratios measured in R_{ax}=3.85m configuration decrease drastically when the island is produced in the ergodic layer, as seen in Fig.14 (d). This reduction of the ratios originates from a simultaneous decrease of CV+CVI and an increase of CIII+CIV (see Figs.14 (e) and (f)).

Edge n_e and T_e profiles are shown in Fig.15 for R_{ax}=3.75 and 3.85m. When the LID coils are turned on in the R_{ax}=3.75m configuration, the T_e profile in the ergodic layer does not change, whereas the T_e profile inside the LCFS changes significantly with this appearance of a flat T_e profile due to an m/n=1/1 island formation (see Fig.15 (b)). In the case of R_{ax}=3.85m, the flat T_e profile expands inside the ergodic layer, as shown in Fig.15 (d). The density in the ergodic layer increases a little when the island is produced (see Fig.15 (c)). Note that the discharges, here produced, had the same line-averaged electron density in both cases with R_{ax}=3.85m. However, a higher gas puffing rate is required when the island is formed. This may be the reason why the ergodic layer density is somewhat high. The reason for the decrease in the density just inside the LCFS with LID for R_{ax}=3.85m is not yet fully understood. The O-point in m/n=1/1 island, formed by LID field, is produced at the outboard side of the #7-O port. The T_e and n_e values from the Thomson scattering diagnostic are measured at port #4-O away from port #7-O by a toroidal angle of 108^0. Therefore, the Thomson diagnostic measures the O-point of the m/n=1/1 island at both the inboard and the outboard side. Here, it should be noted that the LID field can create a magnetic resonance inside the LCFS, but can basically not produce any resonance in the ergodic layer. Figure 15 (d) shows that the island can be created at the inner side of the ergodic layer (R=4.6-4.7m) by activating the LID coils. On the other hand, there exists also a natural island in LHD, probably due to the error field. For the R_{ax}=3.85m configuration, the position of $\iota/2\pi$=1 is located at R=4.57m. The m/n=1/1 natural island has the same toroidal phase as the island produced with the LID coils. Of course, the size of the natural island is considerably smaller than

the LID island. From Fig.15 (d), without activated LID coils, we cannot see any effect of the island in the T_e profile. Therefore, we believe that the n_e decrease in Fig.15 (c) is caused by the island formation with the LID coils. Finally, we note that we have not yet a clear explanation for why the n_e increase at R=4.5m appeared in the case without LID, shown in Fig.15 (c). We also have to examine the edge density profiles with respect to magnetic surface/field deformations due to plasma pressure, temperature effects and the 3-dimensional structure of n_e. The size of the island in the R_{ax}=3.75 and 3.85m configurations is ~17 and ~22cm with T_e ~250 and ~90eV, respectively. From this island experiment one can learn that a modification of the magnetic field lines in the ergodic layer clearly changes the edge impurity transport. To fully understand the parallel and perpendicular transports in the ergodic layer, a more detailed edge transport simulation will be necessary.

D. CARBON EMISSIONS WITH H_2 AND He DISCHARGES

The carbon impurity behavior was also studied by changing the background ion species. For this purpose, He instead of H_2 discharges were produced with the magnetic axis at 3.85m. The ratios of CV+CVI to CIII+CIV are plotted vs $\langle n_e \rangle$ in Fig.16. As shown in Fig.16 (a), the ratios are appreciably reduced in the He discharges, only for densities of $\leq 5\times10^{19}m^{-3}$. This reduction is mainly due to a decrease of CV+CVI intensities, as seen in Fig.16 (b). The CIII+CIV intensities become nearly the same in both cases for densities of $\leq 5\times10^{19}m^{-3}$, except for a sudden rise in the densities for $\geq 5\times10^{19}m^{-3}$ (see Fig.16 (c)).

Waveforms of the line-averaged density are shown in Fig.17 together with the carbon emissions. The global parameters are nearly the same, except for the edge parameters and the carbon emissions. The edge T_e is plotted for ρ=1 as a function of $\langle n_e \rangle$ in Fig.18 (a). No important difference is seen in the figure for the H_2 and He discharges, while the edge T_e in He discharges are somewhat higher. A clear difference is, however, seen in the ion flux measured by Langmuir probe embedded in divertor plates, as shown in Fig.18 (b). If the density in H_2 discharges rises above $n_e=5\times10^{19}m^{-3}$, the ion flux suddenly increases, accompanied by an entirely similar behavior of the

CIII+CIV emission, as shown in Fig.16 (c). In H_2 high-density discharges we see relatively strong emissions from hydrocarbon molecules. We believe that the increase in the carbon emissions in the high-density range is related to the formation of hydrocarbon molecules.

The reduction of the ratio of CV+CVI to CIII+CIV in He discharges seems to be related to a change in the force balance parallel to magnetic fields. Assuming T_i=100eV and $n_i=10^{19}m^{-3}$, the ion-impurity collision frequencies for He-like CV ions are 1.58×10^4 and $3.88\times10^4 s^{-1}$ with H_2 and He background ions, respectively. This leads to an increased friction force. Furthermore, in He plasmas, the constant part of $2.6Z^2$ for the ion thermal force term, given by Eq.1, has to be replaced by $1.6Z^2$. This leads to a reduced contribution from the ion thermal force[23]. The increased friction force and reduced ion thermal force in He plasmas can enhance the impurity screening effect in the ergodic layer. In helical devices, the outside plasma boundary can freely change because the magnetic field for the confinement is given externally. This effect is further enhanced in cases with a thick ergodic layer. The real outside boundary is determined by the thermal balance between the heat input and edge energy losses, such as convective and conductive losses, charge exchange loss, and radiative losses. Especially, the boundary changes in high-density discharges. The edge boundary condition can then easily change from attached to detached plasmas. On the other hand, it is already understood that the fueling efficiency is not good in plasmas with a thick ergodic layer, as shown in Fig.8. Larger gas puffs are necessary to maintain the discharge because of the worse fueling rate. Therefore, the outside plasma boundary can easily be reduced in the high-density range of such a magnetic configuration. The discharges seen in Fig.16 represent the same case. When the plasma radius becomes small in higher density range and the plasma becomes detached, the magnetic field connection length becomes longer at the plasma edge. The perpendicular transport is then more important than the parallel transport. Therefore, we believe that the carbon screening is similar for H_2 and He plasmas at high-density ranges.

VI. COMPARISON WITH SIMULATED CARBON EMISSION USING AN EDGE TRANSPORT CODE

Impurity transport characteristics in the ergodic layer have been analyzed using the three dimensional edge transport code, EMC3-EIRENE. The simulation code EMC3[30] solves the fluid equations of mass, momentum and energy in arbitrary magnetic field geometries, using Monte Carlo scheme. The simulation code of EIRENE[31] solves a kinetic transport model for neutrals, such as the recycling neutrals from divertor plates, and treats the interaction with bulk plasma. The computational domain of the combined code starts from the LCFS upstream, and considers the entire ergodic layer as well as the realistic three dimensional nature of the magnetic field line structure[32].

The profile of the connection length, L_c, in the ergodic layer of LHD, superposed with Poincare plot of field lines, is illustrated in Fig.19 showing two clearly separated regions, the 'stochastic region' and the 'edge surface region'. The values of L_c in range of $1\text{-}10^5$m are plotted in the figure. The magnetic islands are visible in the stochastic region. Moving further outwards, short and long field lines are mixed together. This region, known as the edge surface layer, is characterized by strong magnetic shear, which stretches and bends the flux tubes and thus mixes the long and short flux tubes. The density and energy fluxes at the LCFS obtained from the experiment are used as the boundary conditions for particle and energy transports for an input power of 8MW to SOL, while the Bohm condition is imposed at the divertor plates. The perpendicular transport coefficients, D and χ, for particle and heat fluxes are taken to be 0.5 and $1.5\text{m}^2.\text{s}^{-1}$, respectively. The perpendicular transport coefficient for impurities is considered to be the same as the background ions. For the particle transport, considering a classical parallel convection and anomalous cross-field diffusion, the ratio of parallel to perpendicular transport times is given by[25]

$$\tau_{\parallel} / \tau_{\perp} = 2D / \Delta x \Theta V_{\parallel} , \qquad (7)$$

where D is the cross-field diffusion coefficient, Δx the radial thickness of the ergodic layer, $V_{\parallel}$ the parallel velocity of ions, and Θ the field line pitch inside the remnant islands in the ergodic layer. For $D=0.5\text{m}^2.\text{s}^{-1}$, Δx= several cm, $\Theta=10^{-4}$ and $V_{\parallel}=1.3\times10^5$ m.s^{-1} (the sound speed in a hydrogen plasma with $T_e=T_i=100$eV), the perpendicular and parallel transports become comparable in the ergodic layer of LHD, i.e. $\tau_{\parallel} \sim \tau_{\perp}$. Then, the cross

field transport competes with the parallel transport in LHD. In tokamaks, however, the parallel transport is more dominant than the perpendicular transport.

The obtained impurity density profiles are averaged over the poloidal and toroidal directions in order to plot them as a function of the radial coordinate, r_{eff}, which is defined by a cylindrical approximation of the volume enclosed by each radial surface of the computational mesh. Radial profiles of the total carbon density are plotted in Fig.20 for different plasma densities. Here, n_c/n_{c_ob} is the carbon density normalized to the total carbon density at the outermost boundary of ergodic layer. At the low density of $n_{LCFS}=2\times10^{19}m^{-3}$ the carbon impurity is accumulated towards the LCFS because of the effective ion thermal force. The impurity density in the stochastic layer decreases gradually with increasing densities and the impurity is driven towards the divertor plates due to an increase in the friction force with an increase of n_{LCFS} density.

In the present computational domain a simulation inside the LCFS is difficult. However, a substantial fraction of CVI is often located inside the LCFS. Ratios of CV to CIII+CIV, instead of the ratio of CV+CVI to CIII+CIV, are compared with the simulated ones in Fig.21 (a). Data from the case with the magnetic axis at 3.75m are considered here for comparison. In the intensity calculation of the carbon emissions, the specific volume of observation is determined by each spectrometer, taking into account its observation angle and line-of-sight.

The observed line radiations are plotted in Fig.21 (b) as a function of line-averaged density. The CIII and CIV emissions increase with n_e, whereas the CV emission decreases with n_e. The results from the simulation are shown in Fig.21 (c). The tendency of the predicted emissions is very similar to the experimental ones. However, the absolute magnitudes of the line radiations of CV are clearly different, i.e., the experimental CV radiation is 4 times larger than the calculated one. The reason has not yet been clearly identified. The simulation code makes several assumptions with respect to the complexity of the magnetic field structure in the ergodic layer of LHD and does not access inside the LCFS. Although the magnetic field structure in vacuum is used for the ergodic layer, the deformation due to the plasma pressure is entirely unknown at present. Furthermore, the anomalous pinch effect, which is believed to play an important role in the transport, is not included in the simulation. Some improvements also seem to be

necessary for the absolute calibration of the spectrometers. Therefore, the calculated intensity ratios have been normalized to the experimental ratios. The results are shown in Fig.21 (a). The data have been normalized to the electron density and CIII+CIV emission at $n_e=3.7\times10^{19}m^{-3}$. The n_e dependence of the ratios from the experiment and simulation agree qualitatively well. The simulation was also done for the case of an absent friction force. A clear difference is seen in the behavior of CV, as shown in Fig.21 (d). The CV emission increases monotonically with n_e as well as the CIII and CIV emissions when the friction force is not included in the simulation. As a result, the ratio of CV to CIII+CIV does not decrease with n_e as seen also in Fig.21 (a). The role of the friction force becomes apparent by switching off the friction force term during the simulation.

The carbon density profiles simulated for each charge state are plotted in Fig.22 for two densities at the LCFS. For the high density of $n_{LCFS}=4\times10^{19}m^{-3}$, the impurity ion densities of C^{+4} (CV) and C^{+5} (CVI) become smaller while the ones of C^{+2} (CIII) and C^{+3} (CIV) increase compared with the low-density case. The radial locations of the charge states are not basically changed for different densities. When the density increases, the friction dominant region gradually extends to the inner radial space, which is originally dominated by the ion thermal force. The locations of C^{+2} and C^{+3} are then further limited to the edge surface layer. The negative gradient at $r_{eff}>0.68$m, seen in the total carbon density of Fig.22 (b), is a clear indication for the outward impurity flow and resultant impurity screening.

VII. SUMMARY

Carbon emissions have been studied to understand the impurity behavior in the edge ergodic layer of LHD. The study is carried out by taking the ratio of CV+CVI to CIII+CIV as a typical indicator of the impurity screening. The results are discussed in relation to the impurity transport parallel to the magnetic field lines in the ergodic layer, which is mainly dominated by the ion thermal force and the friction force.

The ratio of CV+CVI to CIII+CIV decreases by two orders of magnitude with increasing n_e in the range of $1–8\times10^{19}m^{-3}$. This result indicates an enhanced impurity screening in the ergodic layer at higher densities, suggesting the importance of the

friction force. The ratio was also examined by changing the thickness of the ergodic layer. The ratio decreases with ergodic layer thickness. The effect of the impurity screening can be enhanced in thicker ergodic layers. The carbon emissions were also observed by changing the radial position of externally supplied m/n=1/1 island. The ratio clearly decreases when the island is located in the ergodic layer. This result evidently indicates that a modification of the magnetic field structure in the ergodic layer has a significant influence on the impurity behavior, although the reason is somewhat unclear because of the uncertainty in the perpendicular transport. The ratio of the carbon impurity emissions is considerably reduced when the H_2 discharge is replaced by a He discharge, except for the high density range, where the ratio seems to increase in helium plasmas. The reduction of the ratio may result from the enhanced friction force due to an increased collision rate with heavier background ions and due to a decreased ion thermal force.

A simulation of the impurity transport in the ergodic layer using EMC3+EIRENE code was done for comparison with the experimental data. The results from this comparison strongly suggest the importance of the friction force in higher density ranges for the appearance of the impurity screening. The density dependence of the simulated ratio of CV to CIII+CIV is in a good agreement with the experimental result. Further efforts are being made to simulate the impurity behavior in the ergodic layer with a large m/n=1/1 island. The dependence of the impurity screening effect on the atomic number is the objective of future experimental and theoretical studies.

Acknowledgements

The authors would like to thank all members of LHD experimental group for their supports during their experimental work. The help of Dr. Tsuguhiro Watanabe in making the drawings of edge magnetic field structure is gratefully acknowledged. This study was performed with financial support by the LHD project (NIFS07ULPP527). This work was also partly supported by the JSPS-CAS Core-University program in the field of 'Plasma and Nuclear Fusion'. Especially one of the authors (S. Morita) would

like to thank Drs. Zhenwei Wu, Yinxian Jie, Zhengying Cui and Baonian Wan for their collaboration and Dr. Manfred Bitter for his English correction.

REFERENCES

[1] C. S. Pitcher and P. C. Stangeby, Plasma Phys. Control. Fusion **39**, 779 (1997).

[2] W. Engelhardt and W. Feneberg, J. Nucl. Mater. **76**, 818 (1978).

[3] Ph Ghendrih, A. Grosman and H. Capes, Plasma Phys. Control. Fusion **38**, 1653 (1996).

[4] T. E. Evans, R. A. Moyer and P. Monat, Phys. Plasmas **9**, 4957 (2002).

[5] J. H. Hogan. C. De Michelis, P. Monier-Garbet, Y. Corre and R. Guirlet, Plasma Phys. Control. Fusion **44**, 673 (2002).

[6] K. H. Finken, T. Eich and A. Kaleck, Nucl. Fusion **38**, 515 (1998).

[7] T. E. Evans, R. A. Moyer, K. H. Burrell, M. E. Fenstermacher, I. Joseph, A. W. Leonard, T. H. Osborne, G. D. Porter, M. J. Schaffer, P. B. Snyder, P. R. Thomas, J. G. Watkins, and W. P. West, Nature Phys. **2**, 419 (2006).

[8] C. Breton, M. Mattioli, C. De Michelis, P. Monier-Garbet, E. Agostini, T. Fall, W. Hess, J. Lasalle, T. E. Evans, A. Grosman, Ph Ghendrih, A.-L. Pecquet, L. Poutchy, A. Samain and J. C. Vallet, Nucl. Fusion **31**, 1774 (1991).

[9] M. Mattioli, C. De Michelis and P. Monier-Garbet, Nucl. Fusion **35**, 807 (1995).

[10] G. Telesca, K. Crombe, M. Tokar, B. Unterberg, G. Verdoolaege, R. Zagorski and G. Van Oost, J. Nucl. Mater. **44**, 337 (2005).

[11] M. Z. Tokar, Phys. Plasmas **6**, 2808 (1999).

[12] S. Morita, T. Morisaki, M. Goto, K. Tankaka, M. B. Chowdhuri, K. Ikeda, R. Katai. S. Masuzaki, K. Nagaoka, K. Narihara, Y. Oka, M. Osakabe, S. Sakakibara, Y. Takeiri, K. Tsumori, H. Yamazaki, K. Y. Watanabe and LHD Experimental Group, Nucl. Fusion **47**, 1033 (2007).

[13] N. Ohyabu, T Watanabe, H. Ji, H. Akao, T. Ono, T. Kawamura, K. Yamazki, K. Akaishi, N. Inoue, A. Komori, Y. Kubota, N. Noda, A Sagara, H. Suzuki, O. Motojima, M. Fujiwara and A. IIyoshi, Nucl. Fusion **34**, 387 (1994).

[14] S. Morita, M. Goto, S. Muto, R. Katai, H. Yamazaki, H. Nozato, A Iwamae, M. Atake, T. Fujimoto, A. Sakaue, H. Nishimura, I. Sakurai, C. Matsumoto, A. Furuzawa, Y. Tawara, M. Aramaki, Y. Okumura, K. Sasaki, G. Xianzu, Li Jiangang, W. Baonian and C. Zhengying, Plasma Sci. Tech **8**, 55 (2006).

[15] S. Morita, M. Goto, T. Morisaki, S. Inagaki, M. Emoto, H. Funaba, K. Ida, H. Idei, S. Kado, O. Kaneko, K. Kawahata, T. Kobuchi, A. Komori, S. Kubo, R. Kumazawa, S. Masuzaki, T. Minami, J. Miyazawa, O. Motojima, S. Murakami, S. Muto, T. Mutoh, Y. Nagayama, Y. Nakamura, H. Nakanisi, K. Narihara, K. Nishimura, N. Noda, S. Ohdachi, N. Ohyabu, Y. Oka, M. Osakabe, T. Ozaki, B.J. Peterson, A. Sagara, S. Sakakibara, R. Sakamoto, H. Sasao, K. Sato, M. Sato, T. Seki, T. Shimozuma, Y. Shirai, M. Shoji, T. Sugie, H. Suzuki, Y. Takeiri, K. Tanaka, K. Toi, T. Tokuzawa, K. Tsumori, K. Tsuzuki, B. N .Wan, K .Y. Watanabe, T. Watari, I. Yamada, H. Yamada, and S. Yamaguchi, *Proc. 26th. European Conference on Controlled Fusion and Plasma Physics*, Maastricht, 1999 (European Physical Society, Geneva, 1999) Vol.23J, p.1321.

[16] N. Ohyabu, A. Komori, H. Suzuki, T. Morisaki, S. Masuzaki, H Funaba, N. Noda, Y. Nakamura, A. Sagara, N. Inoue, R. Sakamoto, S. Inagaki, S. Morita, Y. Takeiri, T, Watanabe, Y, Matsumoto, O. Motojima, M. Fujiwara and A. Iiyoshi, J. Nucl. Mater. **266-269**, 302 (1999).

[17] S. Masuzaki, T. Morisaki, N. Ohyabu, A. Komori, H. Suzuki, N. Noda, Y. Kubota, R. Sakamoto, K. Narihara, K. Kawahata, K. Tanaka, T. Tokuzawa, S. Morita, M. Goto, M. Osakabe, T. Watanabe, Y. Matsumoto, O. Motojima and the LHD Experimental group, Nucl. Fusion **42**, 750 (2002).

[18] T. Morisaki, K. Narihara, S. Masuzaki, S. Morita, M. Goto, A. Komori, N. Ohyabu, O. Motojima, K. Matsuoka and LHD Experimental Group, J. Nucl. Mater. **313-316**, 548 (2003).

[19] S. Morita, M. Goto, H. Funaba, H. Idei, K. Ikeda, S. Inagaki, O. Kaneko, K. Kawahata, A. Komori, S. Kubo, R. Kumazawa, S. Masuzaki, J. Miwazawa, T. Morisaki, O. Motojima, S. Muto, T. Mutoh, Y. Nakamura, K. Narihara, K. Nishimura, N. Noda, S. Ohdachi, N. Ohyabu, Y. Oka, M. Osakabe, A. Sagara, S. Sakakibara, R. Sakamoto, T. Seki, T. Shimozuma, M. Shoji, Y. Takeiri, K. Tanaka, K. Toi, T. Tokuzawa, K. Tsumori, H. Yamada. K. Y. Watanabe and T. Watari, Physica Script **T91**, 48 (2001).

[20] M. B. Chowdhuri, S. Morita, M. Goto, H. Nishimura, K. Nagai and S. Fujioka, Rev. Sci. Instrum. **78**, 023501 (2007).

[21] M. B. Chowdhuri, S. Morita and M. Goto, Appl. Opt. **47**, 136 (2008).

[22] H. Zhou, S. Morita, M. Goto, and M. B. Chowdhuri, Rev. Sci. Instrum. **79,** 10F536 (2008).

[23] P. C. Stangeby, *The Plasma Boundary of Magnetic Fusion Devices*, chapter 6, (Institute for Physics Publishing, 2002).

[24] M. Kobayashi, Y. Feng, S. Masuzaki, T. Morisaki, N. Ohyabu, H. Yamada. O. Motojima and LHD Experimental Group, Contrib. Plasma Phys. **48**, 255 (2008).

[25] Y. Feng, F. Sardei, P. Grigull, K. McCormick, J. Kisslinger and D. Reiter, Nucl. Fusion **46**, 807 (2006).

[26] T. Amano, J. Mizuno, and T. Kako, Int. Rep. IIPJ-616, (Institute for Plasma Physics, Nagoya University, 1982).

[27] H. Nozato, S. Morita, M. Goto, Y. Takase, A Ejiri, T. Amano, K. Tanaka, S. Inagaki and LHD Experimental Group, Phys. Plasmas **13**, 092502 (2006).

[28] M. Goto, and S. Morita, Phys. Rev. E **65**, 026401 (2002).

[29] H. Yamazaki, M. Goto, S. Morita, T. H. Watanabe and LHD Experimental Group, Plasma Fusion Res. **2**, S1000 (2007).

[30] Y. Feng, F. Sardei, J. Kisslinger, P. Gigolo, K. McCormick and D. Reiter, Contrib. Plasma Phys. **44**, 57 (2004).

[31] D. Reiter, M. Baelmans and P. Borner, Fusion Sci. Technol. **47**, 172 (2005).

[32] M. Kobayashi, Y. Feng, S. Morita, K. Sato, M. B. Chowdhuri, S. Masuzaki, M. Shoji, Y. Nakamura, M. Tokitani, N. Ohyabu, M. Goto, T. Morisaki, I. Yamada, K. Narihara, N. Ashikawa, H. Yamada, A. Komori, O. Motojima and the LHD Experimental Group, Plasma Fusion Res. **3**, S1005 (2008).

FIGURE CAPTIONS

Fig.1. Schematic views of horizontally elongated plasma cross section in (a) R_{ax}=3.6 and (b) 4.0m of LHD. Major radius and vertical distance are indicated by R and Z, respectively. The equatorial plane is at Z=0.

Fig.2. Edge profiles of magnetic field connection length, L_c, at outboard side of horizontally elongated plasma cross section as a function of major radius, R, for (a) R_{ax}=3.6 and (b) 4.0m. Vertical solid lines indicate LCFS positions and horizontal thick bars denote range of ergodic layer.

Fig.3. Fractional abundance of C^{+}, C^{+2}, C^{+3}, C^{+4}, C^{+5} and C^{+6} as a function of T_e.

Fig.4. Vertical profiles of (a) CIII (4647Å), (b) CIV (5810Å) and (c) CV (2271Å) at R_{ax}=3.6m, measured by spectrometer for measurements of visible bremsstrahlung profile.

Fig.5. Viewing chords of visible bremsstrahlung spectrometer (horizontal lines) and magnetic field structure of LHD for R_{ax}=3.6m. The symbol '#41' represents the number of optical fibers.

Fig.6. (a) Ratio of CV+CVI to CIII+CIV and (b) normalized intensities of (CV+CVI)/n_e (closed circles) and (CIII+CIV)/n_e (open triangles) in unit of 10^{14} photons.cm^{-2}.sr^{-1}.s^{-1}/ 10^{19}m^{-3} as a function of $<n_e>$ for R_{ax}=3.6m.

Fig.7. (a) Edge n_e and (b) T_e profiles as a function of major radius for low-density (closed circles: $<n_e>$=1.50x10^{19}m^{-3}) and high-density (open triangles: 5.52×10^{19}m^{-3}) discharges for R_{ax}=3.6m.

Fig.8. (a) Ratio of CV+CVI to CIII+CIV and normalized intensities of (b) (CV+CVI)/n_e and (c) (CIII+CIV)/n_e in unit of 10^{14} photons.cm^{-2}.sr^{-1}.s^{-1}/10^{19}m^{-3} as a function of $<n_e>$

for R_{ax}=3.60 (closed circles), 3.75 (open diamonds), 3.90 (closed squares) and 4.00m (open triangles).

Fig.9. Edge profiles of magnetic field connection length, L_c, plotted as a function of major radius, R, at inboard (a)-(d) and outboard (e)-(f) sides of horizontally elongated plasma cross section in R_{ax}=3.60, 3.75, 3.90 and 4.00m, respectively. Vertical solid lines indicate LCFS positions and horizontal thick bars denoted with 'Erg' show the range of ergodic layer.

Fig.10. Ergodic layer thickness, λ_{erg}, as function of magnetic axis, R_{ax}, at inboard (closed circles) and outboard (open triangles) sides in horizontally elongated plasma cross section.

Fig.11. (a) Edge n_e and (b) T_e profiles as a function of major radius for R_{ax}=3.60 (closed circles) and 4.00m (open triangles). Vertical lines indicate LCFS positions for R_{ax}=3.60 and 4.00m.

Fig.12. Radial profiles of rotational transform, $\iota/2\pi$, for R_{ax}=3.60 (—), 3.75 (– – –), 3.85 (· – · –), 3.90 (– —) and 4.00m (·····). Value of ρ is the normalized radius.

Fig.13. Magnetic field structures of edge ergodic layer for horizontally elongated plasma cross sections for (a) R_{ax}=3.75m without LID, (b) R_{ax}=3.75m with LID, (c) R_{ax}=3.85m without LID and R_{ax}=3.85m with ILD. Large m/n=1/1 island is externally produced by ten sets of LID coils. Vertical solid lines indicate LCFS positions.

Fig.14. (a) Ratio of CV+CVI to CIII+CIV and normalized intensities of (b) (CV+CVI)/n_e and (c) (CIII+CIV)/n_e as a function of $<n_e>$ for R_{ax}=3.75m and (d) ratio of CV+CVI to CIII+CIV emissions, normalized intensities of (e) (CV+CVI)/n_e and (f) (CIII+CIV)/n_e as a function of $<n_e>$ for R=3.85m without (closed circles) and with (open triangles) LID coils current. (CV+CVI)/n_e and (CIII+CIV)/n_e are given in units of 10^{14} photons.cm^{-2}.sr^{-1}.s^{-1}/10^{19}m^{-3}.

Fig.15. Edge n_e and T_e profiles as a function of major radius with (open triangles) and without (closed circles) LID; (a) n_e at R_{ax}=3.75, (b) T_e at R_{ax}=3.75, (c) n_e at R_{ax}=3.85m and (d) T_e at R_{ax}=3.85m. Solid vertical lines indicate LCFS positions.

Fig.16. (a) Ratio of CV+CVI to CIII+CIV and normalized intensities of (b) (CV+CVI)/n_e and (c) (CIII+CIV)/n_e in unit of 10^{14} photons.cm^{-2}.sr^{-1}.s^{-1}/10^{19}m^{-3} as a function of $<n_e>$ for H_2 (closed circles) and He (open triangles) discharges.

Fig.17. (a) Line-averaged density, $<n_e>$ and normalized intensities of (b) CIII/n_e, (c) CIV/n_e, (d) CV/n_e and (e) CVI/n_e in H_2 (solid lines) and He (dashed lines) discharges. Unit for carbon emissions of CIII (977Å), CIV (1548Å), CV (40.27Å) and CVI (33.73Å) is 10^{14} photons.cm^{-2}.sr^{-1}.s^{-1}/10^{19}m^{-3}.

Fig.18. (a) T_e at ρ=1 and (b) divertor ion saturation current, I_{sat}, as a function of $<n_e>$ for H_2 (closed circles) and He (open triangles) discharges.

Fig.19 (Color online). Two-dimensional profile of connection length, L_c, in ergodic layer of LHD (R_{ax}=3.75m) superposed with Poincare plot of magnetic field lines.

Fig.20. Edge profiles of carbon density summed over all charge states for different densities: (a) $n_{LCFS}=2\times10^{19}$m^{-3} (dotted line), 3×10^{19}m^{-3} (dashed line) and 4×10^{19}m^{-3} (solid line). n_c/n_{c_ob} is carbon density normalized to the total carbon density at outermost boundary of ergodic layer. Horizontal axis represents minor radius r_{eff} which is defined by cylindrical approximation. Vertical dashed line indicates the boundary between stochastic region and edge surface layers as shown in Fig.19.

Fig.21. (a) Ratios of CV to CIII+CIV from experiment (closed circles) and simulation with (open triangles+solid line) and without (open diamonds+dotted line) friction force as a function of $<n_e>$ and normalized line radiations of CIII/n_e (closed circles), CIV/n_e (open diamonds) and CV/n_e (closed triangles) from (b) experiment and simulations (c) with and

(d) without friction force in unit of $kW/10^{19}m^{-3}$ as a function of $<n_e>$. Ratios from simulation are normalized to experimental value of $3.7\times10^{19}m^{-3}$.

Fig.22. Radial carbon density profiles of each charge state simulated by EMC3-EIRENE code with (a) $n_{LCFS}=2\times10^{19}$ and (b) $4\times10^{19}m^{-3}$. Solid vertical arrows indicate position of LCFS for R_{ax}=3.75m.

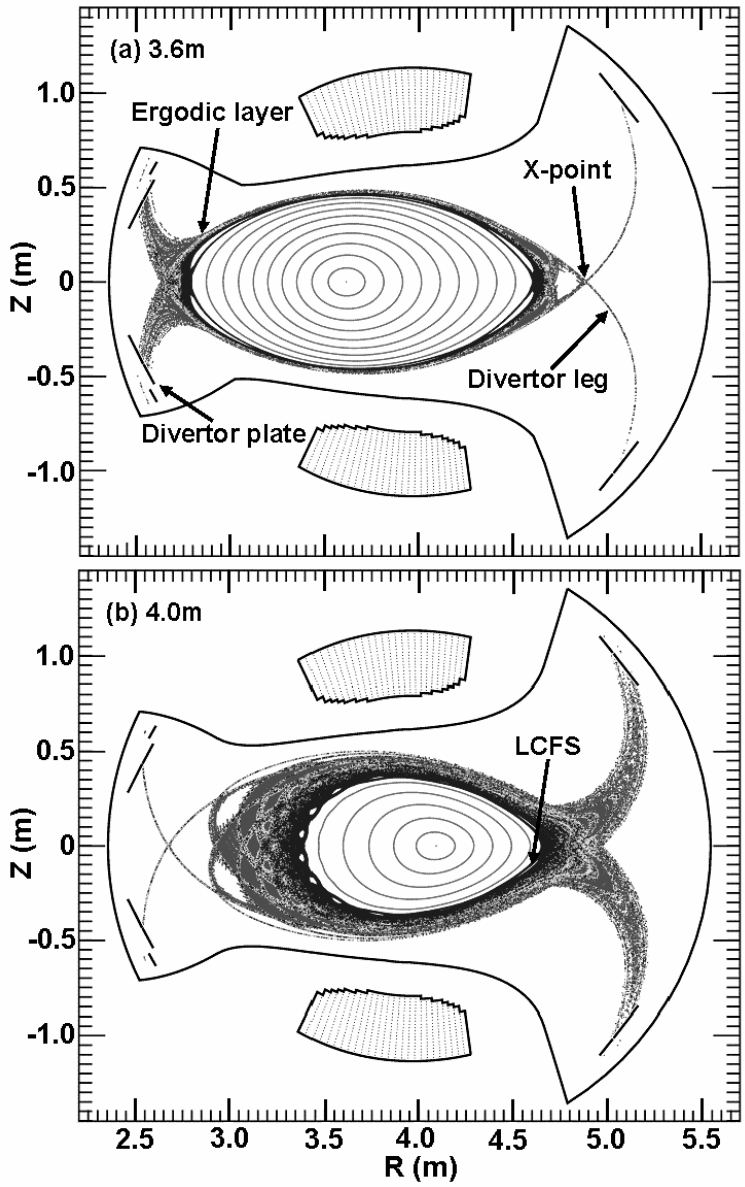

Fig.1. Schematic views of horizontally elongated cross section in (a) R_{ax}=3.6 and (b) 4.0m of LHD. Major radius and vertical distance are indicated by R and Z, respectively. The equatorial plane is at Z=0.

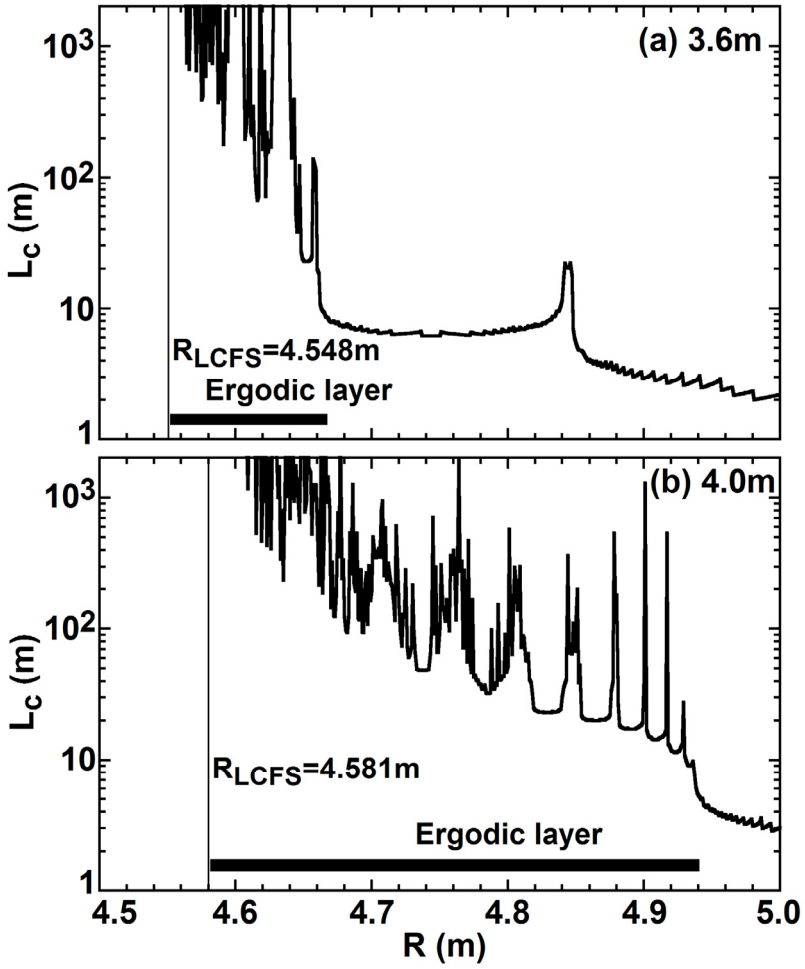

Fig.2. Edge profiles of magnetic field connection length, L_c, at outboard side in horizontally elongated cross section as a function of major radius, R, for (a) R_{ax}=3.6 and (b) 4.0m. Vertical solid lines indicate the LCFS positions and horizontal thick bars show the ergodic layer region.

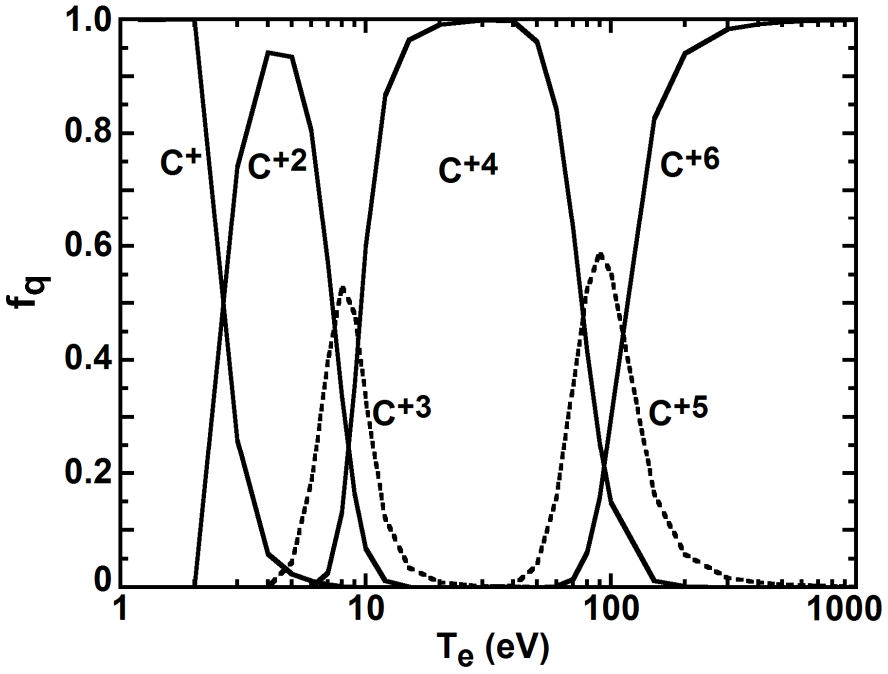

Fig.3. Fractional abundance of C^{+}, C^{+2}, C^{+3}, C^{+4}, C^{+5} and C^{+6} as a function of T_e.

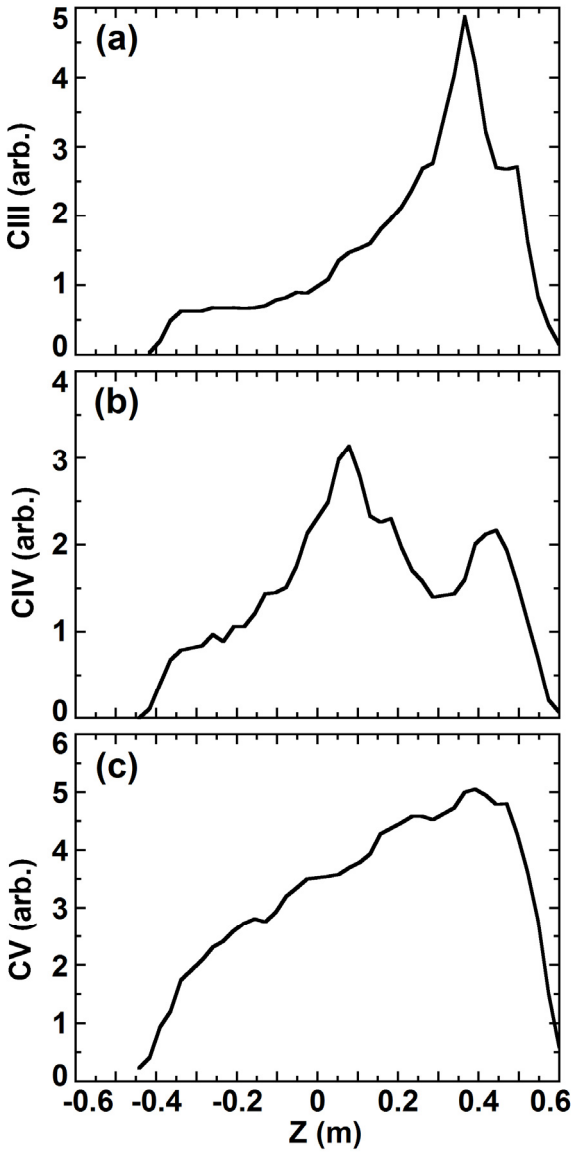

Fig.4. Vertical profiles of (a) CIII (4647Å), (b) CIV (5810Å) and (c) CV (2271Å) at R_{ax}=3.6m measured by spectrometer for measurements of visible bremsstrahlung profile.

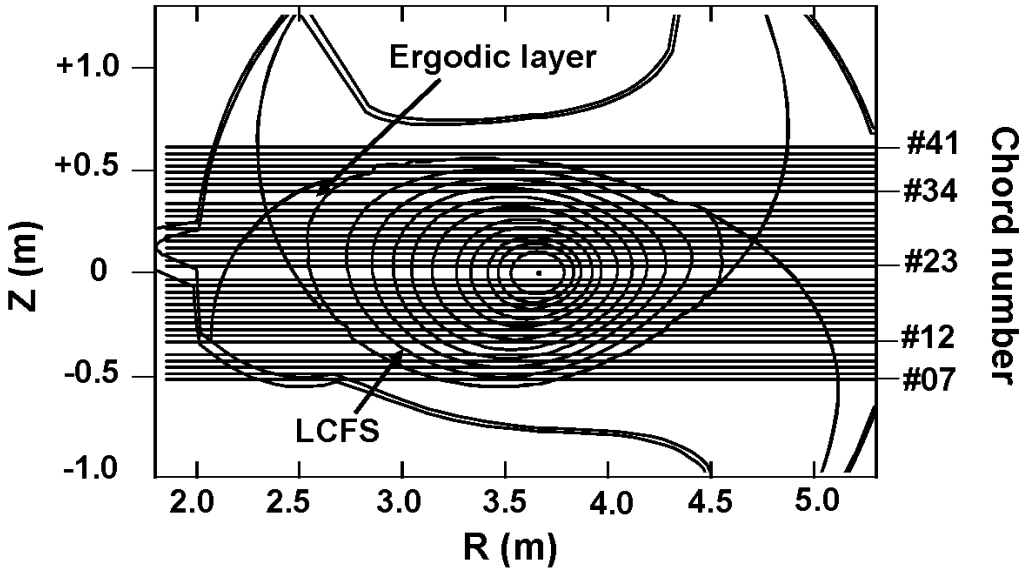

Fig.5. Viewing chords of visible bremsstrahlung spectrometer (horizontal lines) and magnetic field structure of LHD for R_{ax}=3.6m. The symbol '#41' represents the number of optical fibers.

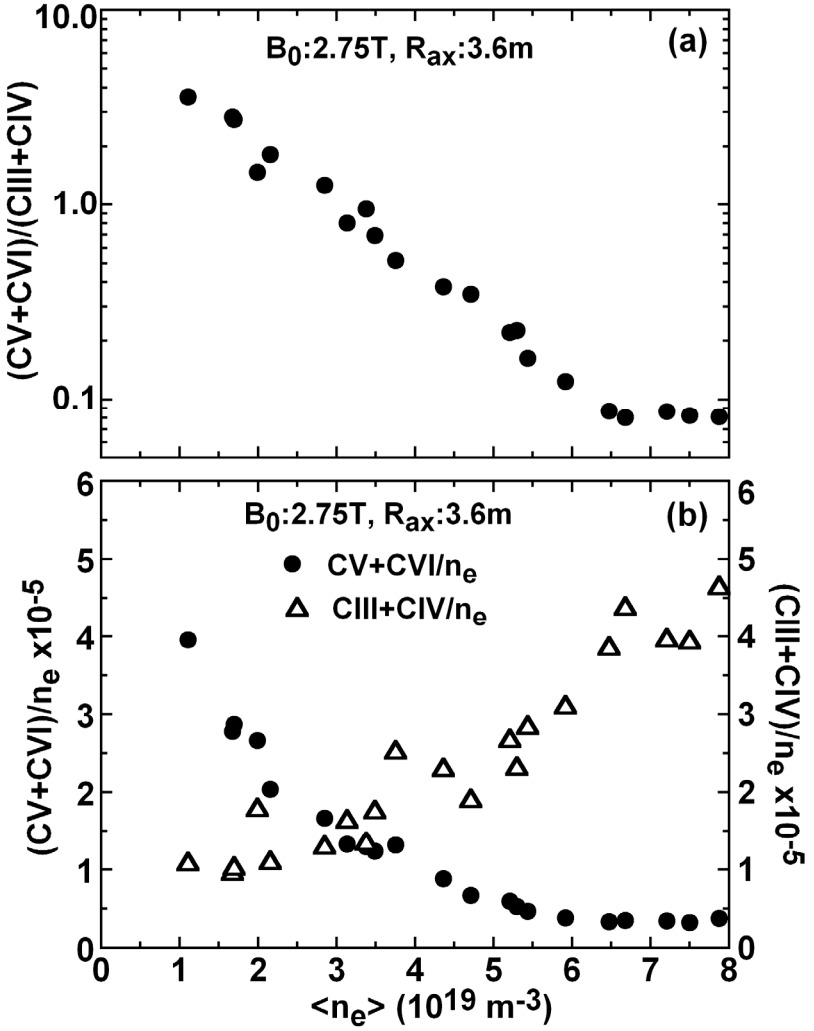

Fig.6. (a) Ratio of CV+CVI to CIII+CIV and (b) normalized intensities of (CV+CVI)/n_e (closed circles) and (CIII+CIV)/n_e (open triangles) in unit of 10^{14} photons.cm^{-2}.sr^{-1}.s^{-1}/10^{19}m^{-3} as a function of $<n_e>$ for R_{ax}=3.6m.

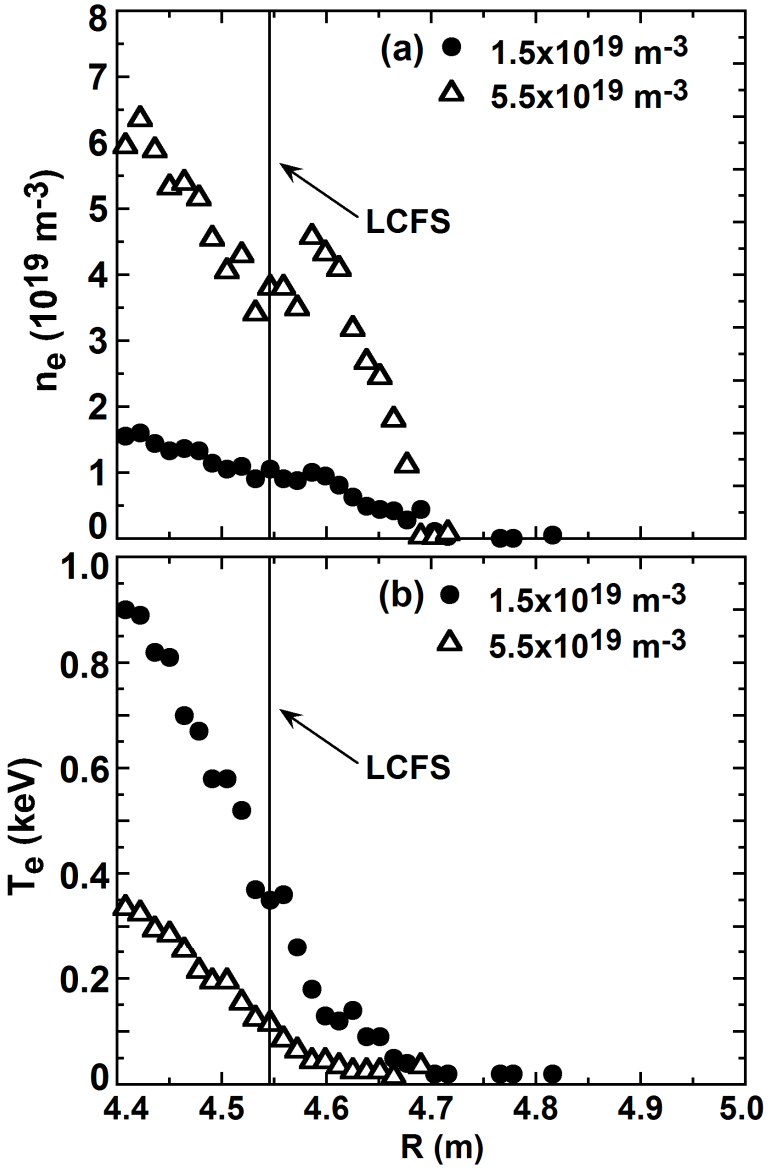

Fig.7. (a) Edge n_e and (b) T_e profiles as a function of major radius for low-density (closed circles: $<n_e>=1.50\text{x}10^{19}m^{-3}$) and high-density (open triangles: $5.52\times10^{19}m^{-3}$) discharges for R_{ax}=3.6m.

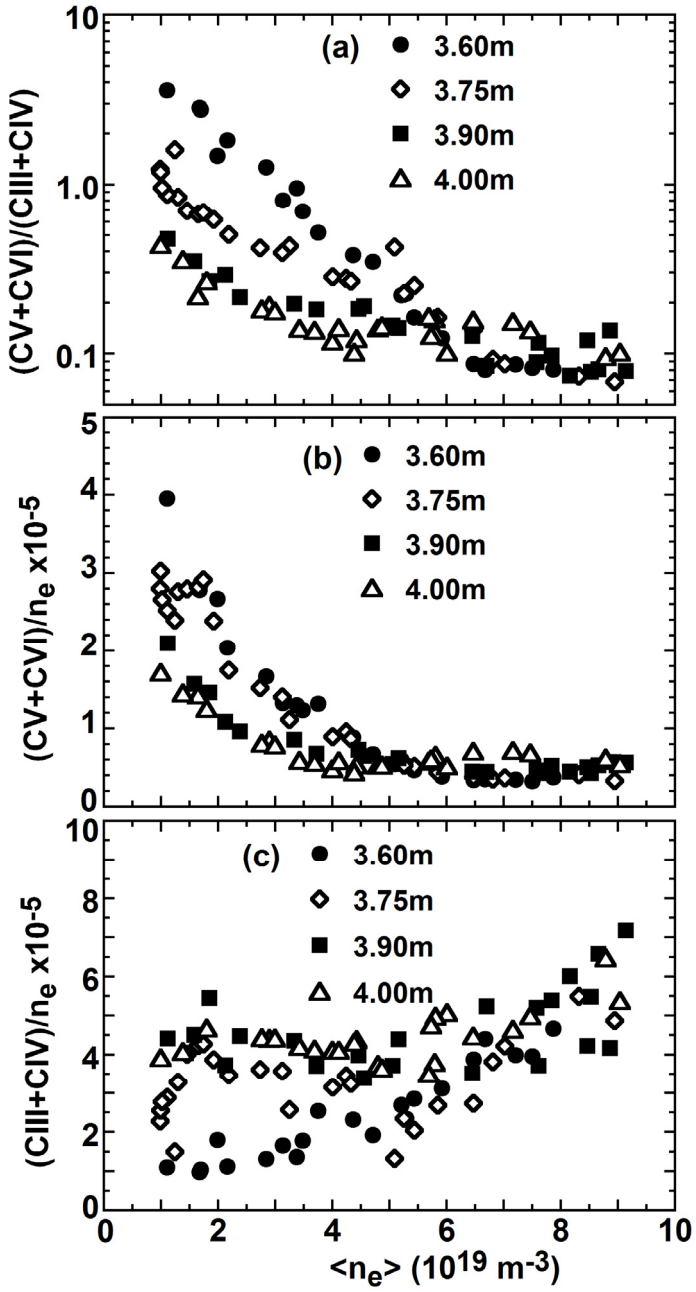

Fig.8. (a) Ratio of CV+CVI to CIII+CIV and normalized intensities of (b) (CV+CVI)/n_e and (c) (CIII+CIV)/n_e in unit of 10^{14} photons.cm^{-2}.sr^{-1}.s^{-1}/10^{19}m^{-3} as a function of $\langle n_e \rangle$ for R_{ax}=3.60 (closed circles), 3.75 (open diamonds), 3.90 (closed squares) and 4.00m (open triangles).

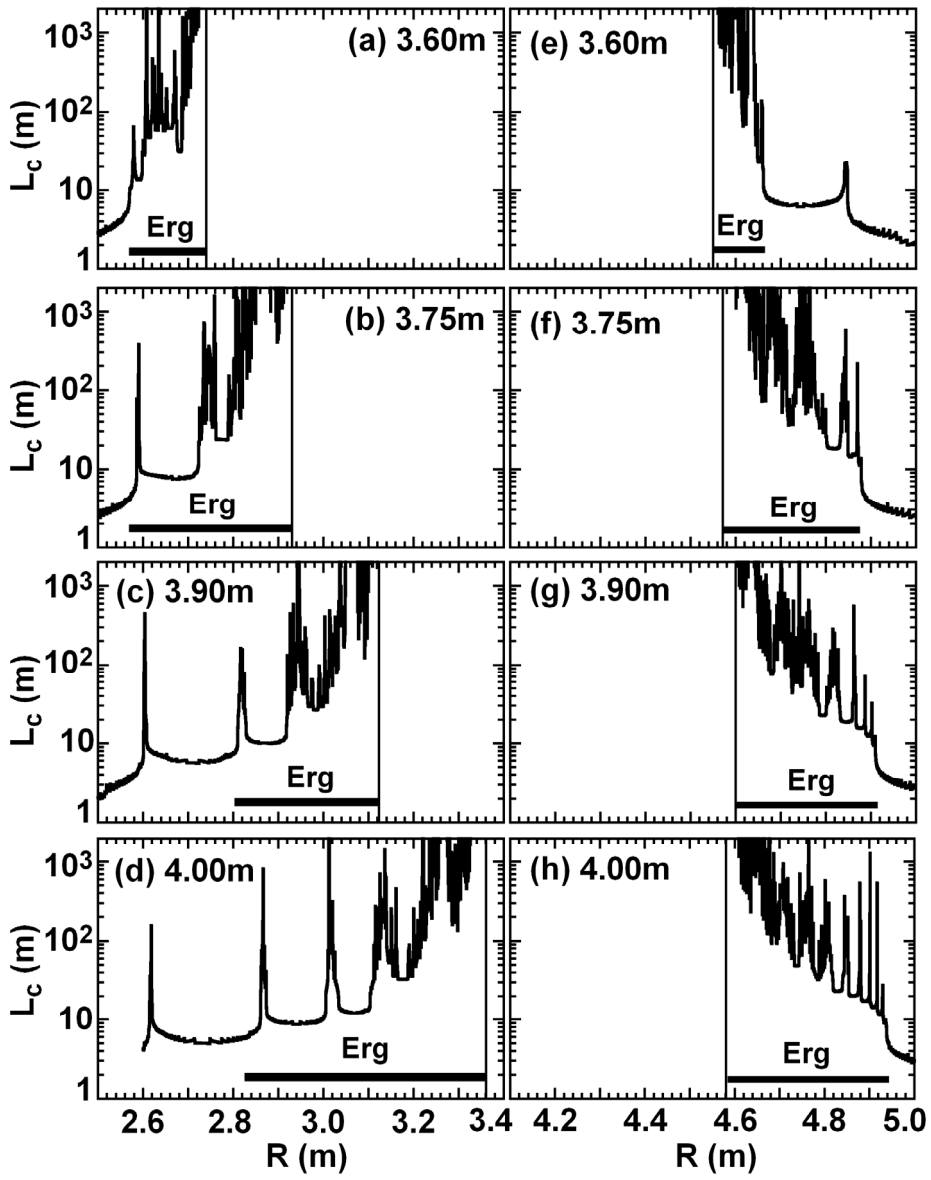

Fig.9. Edge profiles of magnetic field connection length, L_c, plotted as a function of major radius, R, at inboard (a)-(d) and outboard (e)-(f) sides of horizontally elongated cross section in R_{ax}=3.60, 3.75, 3.90 and 4.00m, respectively. Vertical solid lines indicate LCFS positions and horizontal thick bars denoted with 'Erg' show the range of ergodic layer.

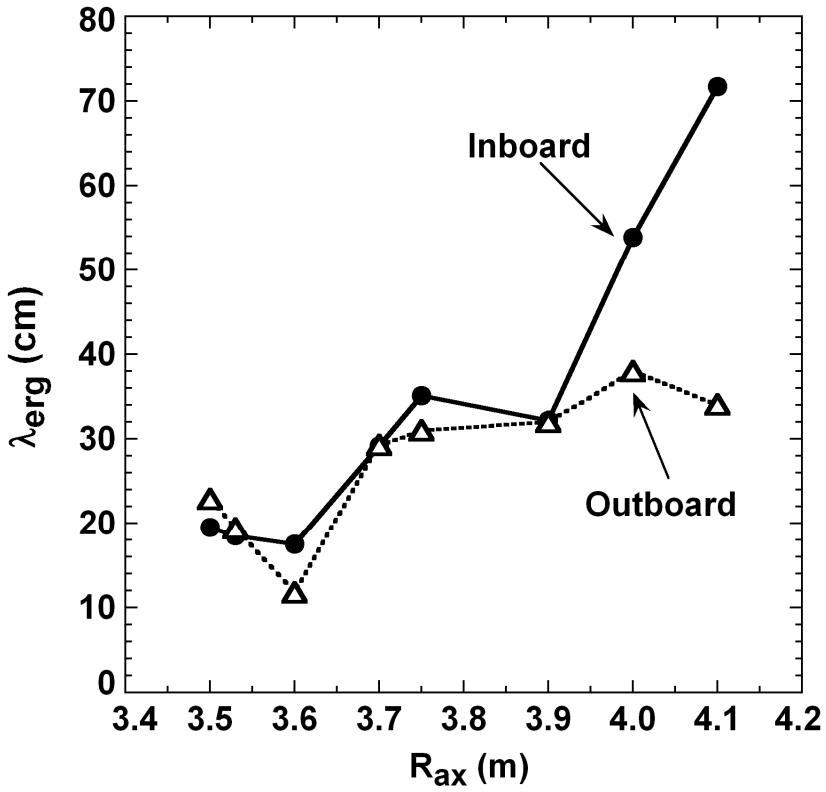

Fig.10. Ergodic layer thickness, λ_{erg}, as function of magnetic axis, R_{ax}, at inboard (closed circles) and outboard (open triangles) sides in horizontally elongated plasma cross section.

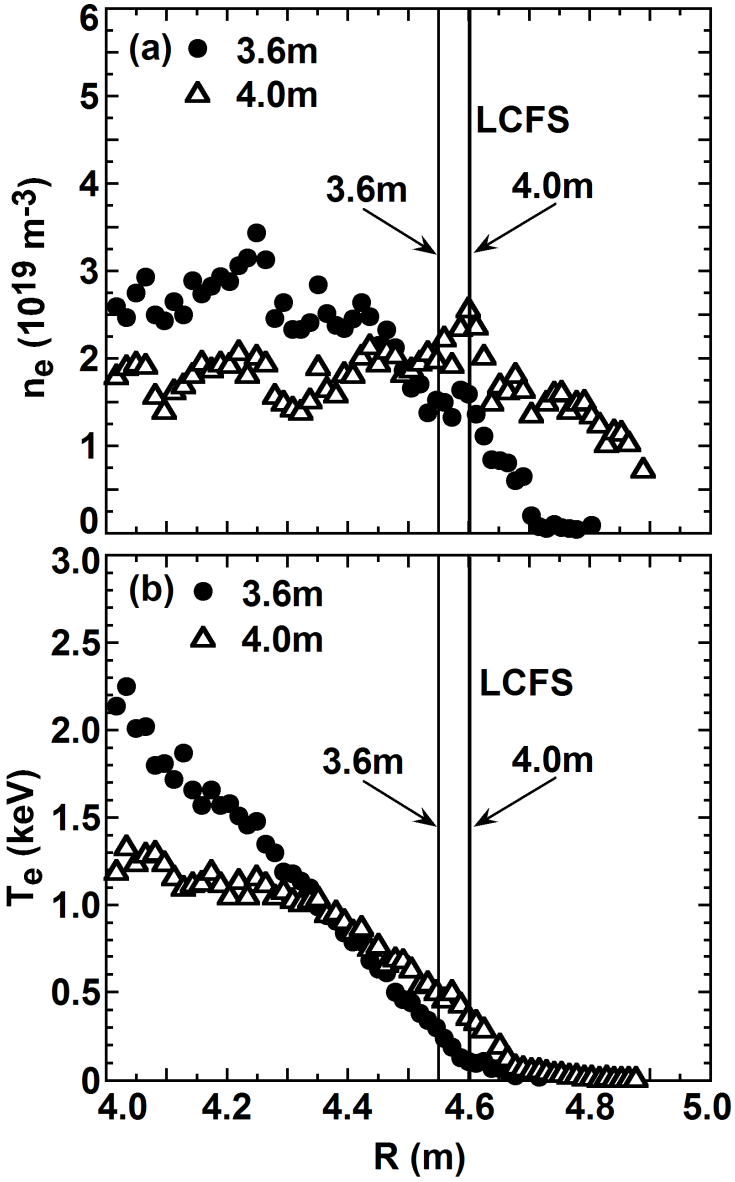

Fig.11. (a) Edge n_e and (b) T_e profiles as a function of major radius for R_{ax}=3.60 (closed circles) and 4.00m (open triangles). Vertical lines indicate LCFS positions for R_{ax}=3.60 and 4.00m.

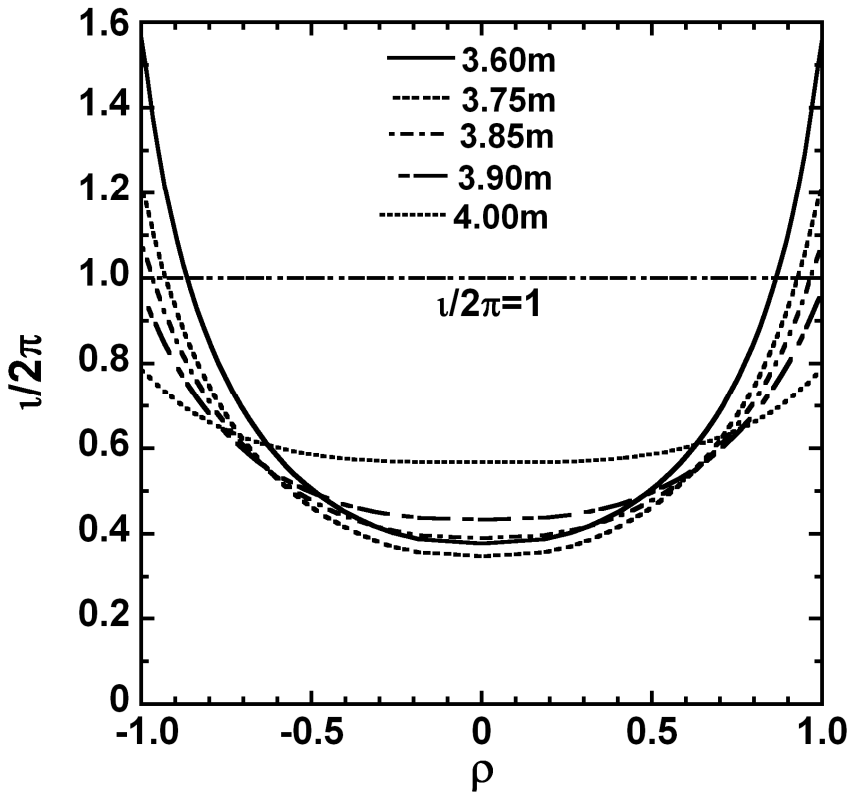

Fig.12. Radial profiles of rotational transform, ι/2π, for R_{ax}=3.60 (—), 3.75 (– – –), 3.85 (· – · –), 3.90 (– —) and 4.00m (·····). Value of ρ is the normalized radius.

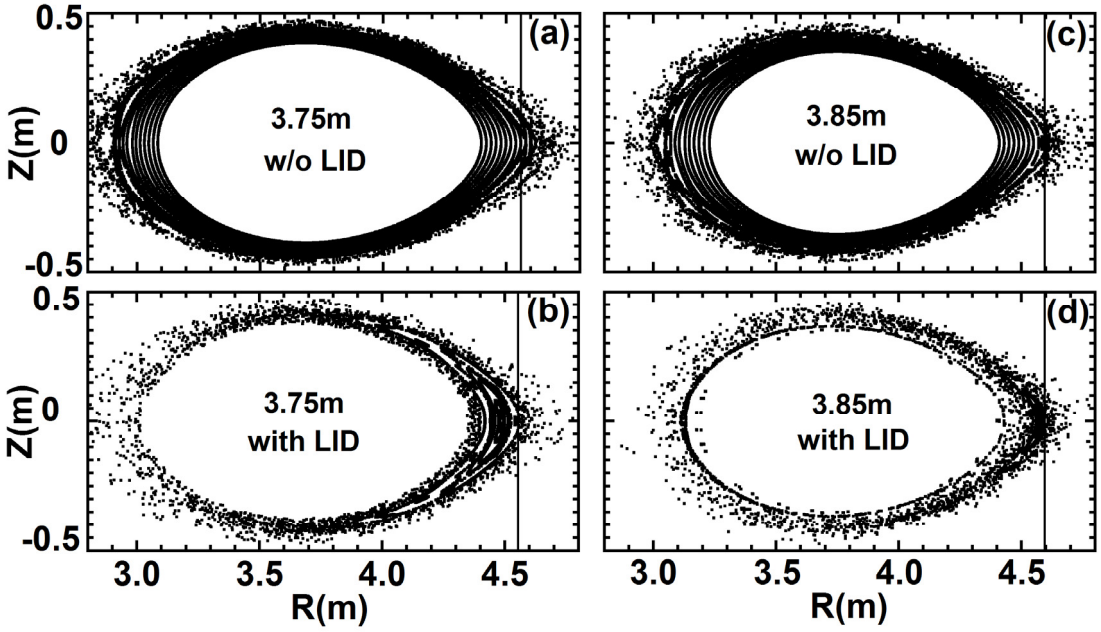

Fig.13. Magnetic field structures of edge ergodic layer for horizontally elongated cross sections for (a) R_{ax}=3.75m without LID, (b) R_{ax}=3.75m with LID, (c) R_{ax}=3.85m without LID and R_{ax}=3.85m with ILD. Large m/n=1/1 island is externally produced by ten set of LID coils. Vertical solid lines indicate LCFS positions.

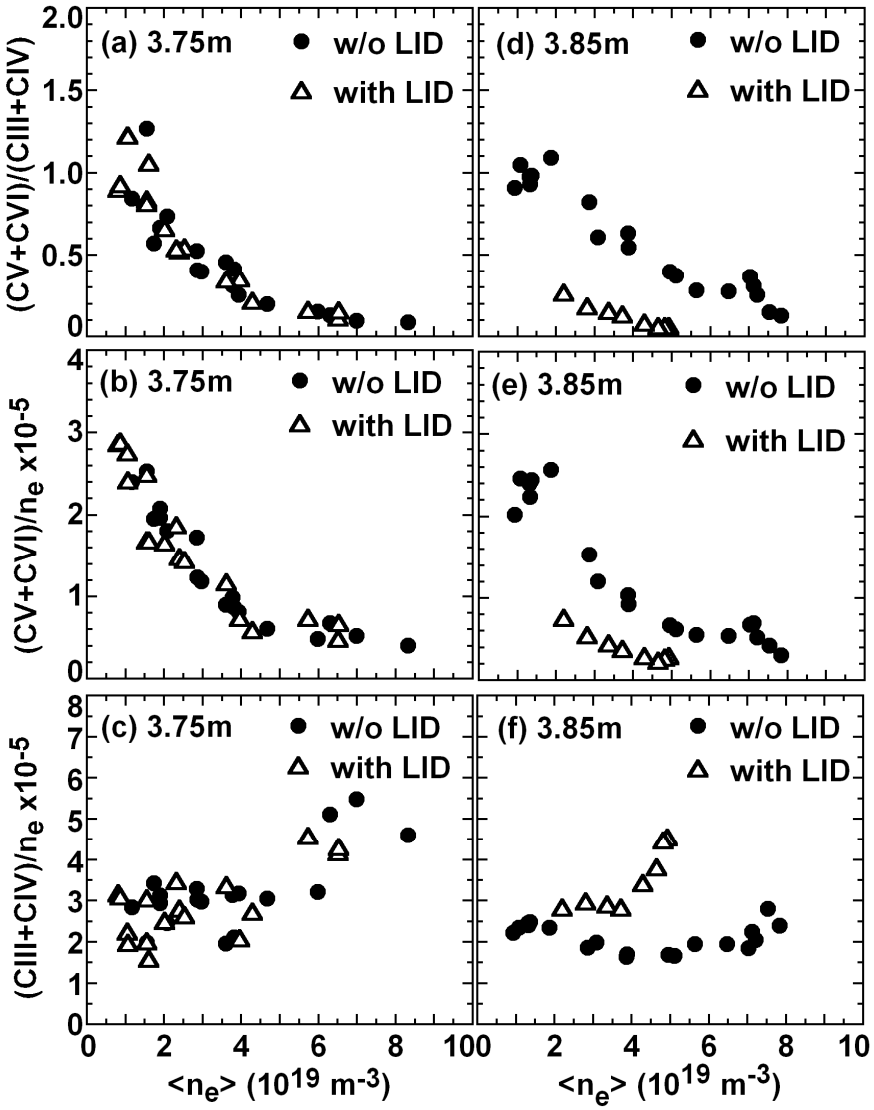

Fig.14. (a) Ratio of CV+CVI to CIII+CIV and normalized intensities of (b) $(CV+CVI)/n_e$ and (c) $(CIII+CIV)/n_e$ as a function of $\langle n_e \rangle$ for R_{ax}=3.75m and (d) ratio of CV+CVI to CIII+CIV emissions, normalized intensities of (e) $(CV+CVI)/n_e$ and (f) $(CIII+CIV)/n_e$ as a function of $\langle n_e \rangle$ for R=3.85m without (closed circles) and with (open triangles) LID coils current. $(CV+CVI)/n_e$ and $(CIII+CIV)/n_e$ are given in units of 10^{14} photons.cm^{-2}.sr^{-1}.s^{-1}/10^{19}m^{-3}.

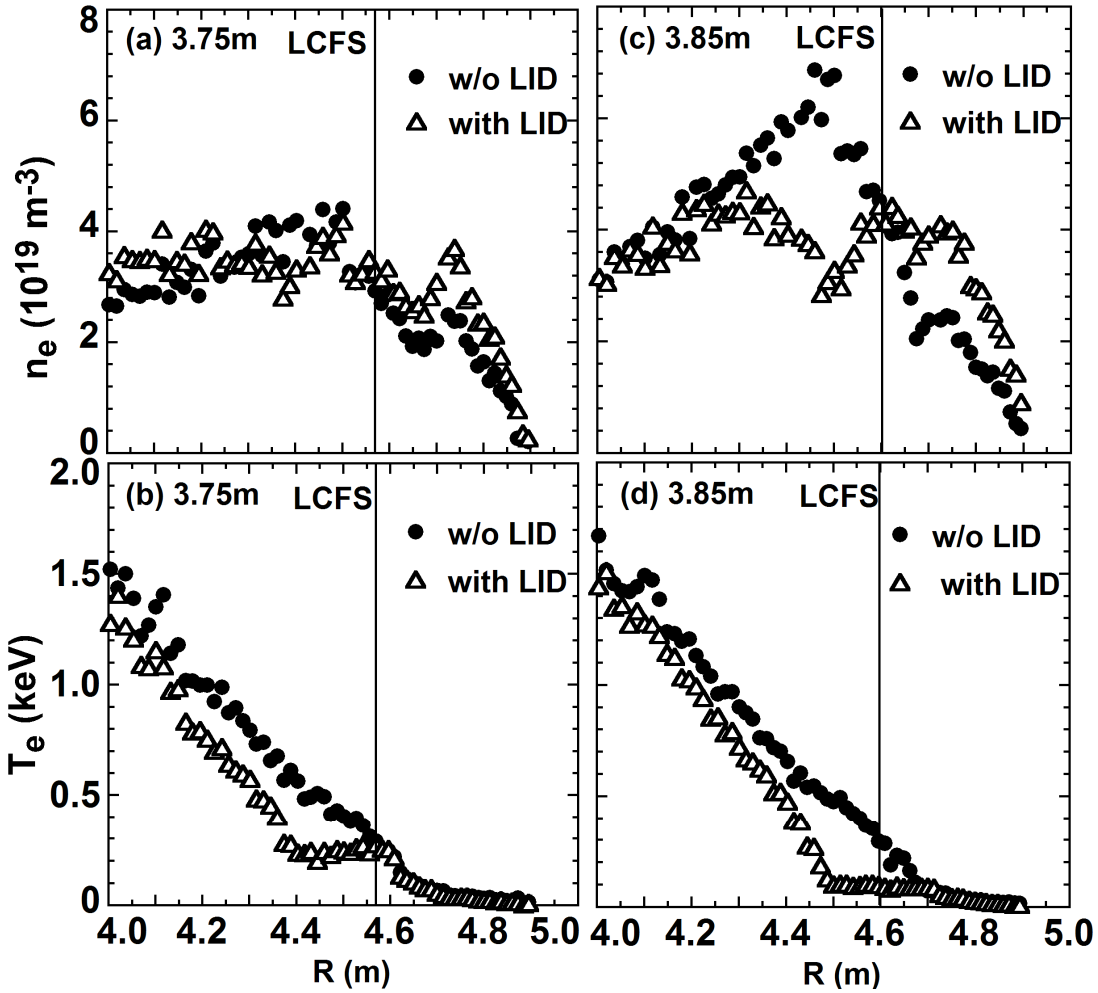

Fig.15. Edge n_e and T_e profiles as a function of major radius with (open triangles) and without (closed circles) LID; (a) n_e at R_{ax}=3.75, (b) T_e at R_{ax}=3.75, (c) n_e at R_{ax}=3.85m and (d) T_e at R_{ax}=3.85m. Solid vertical lines indicate LCFS positions.

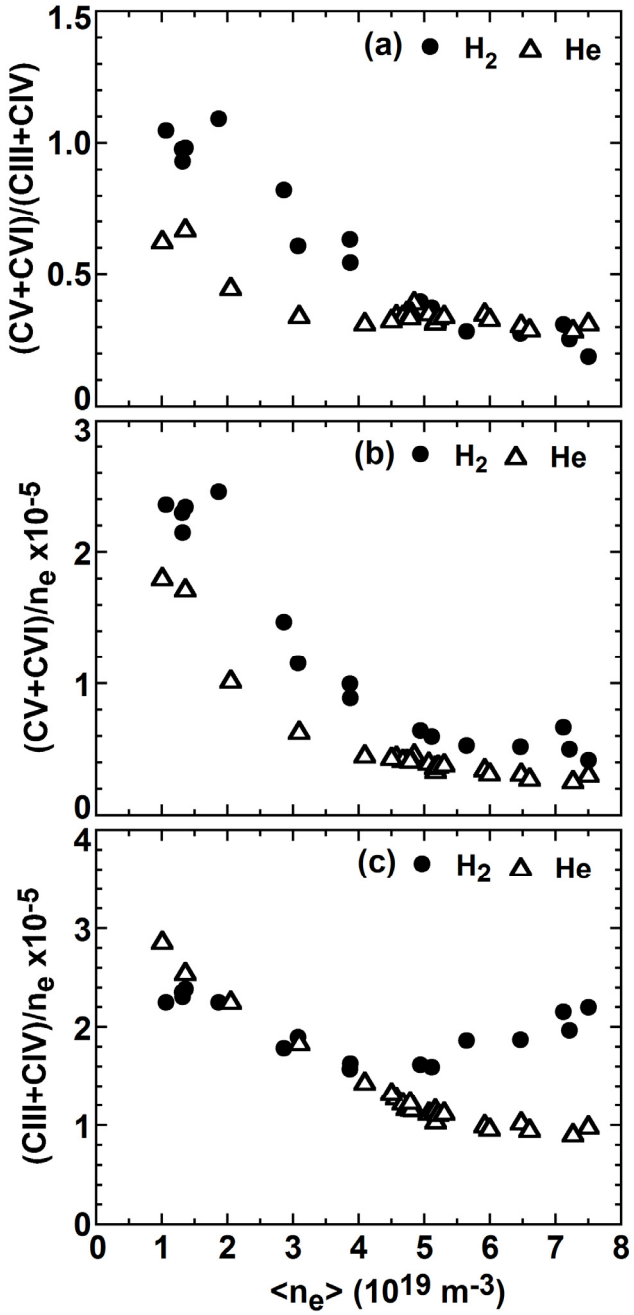

Fig.16. (a) Ratio of CV+CVI to CIII+CIV and normalized intensities of (b) (CV+CVI)/n_e and (c) (CIII+CIV)/n_e in unit of 10^{14} photons.cm^{-2}.sr^{-1}.s^{-1}/10^{19}m^{-3} as a function of $\langle n_e \rangle$ for H_2 (closed circles) and He (open triangles) discharges.

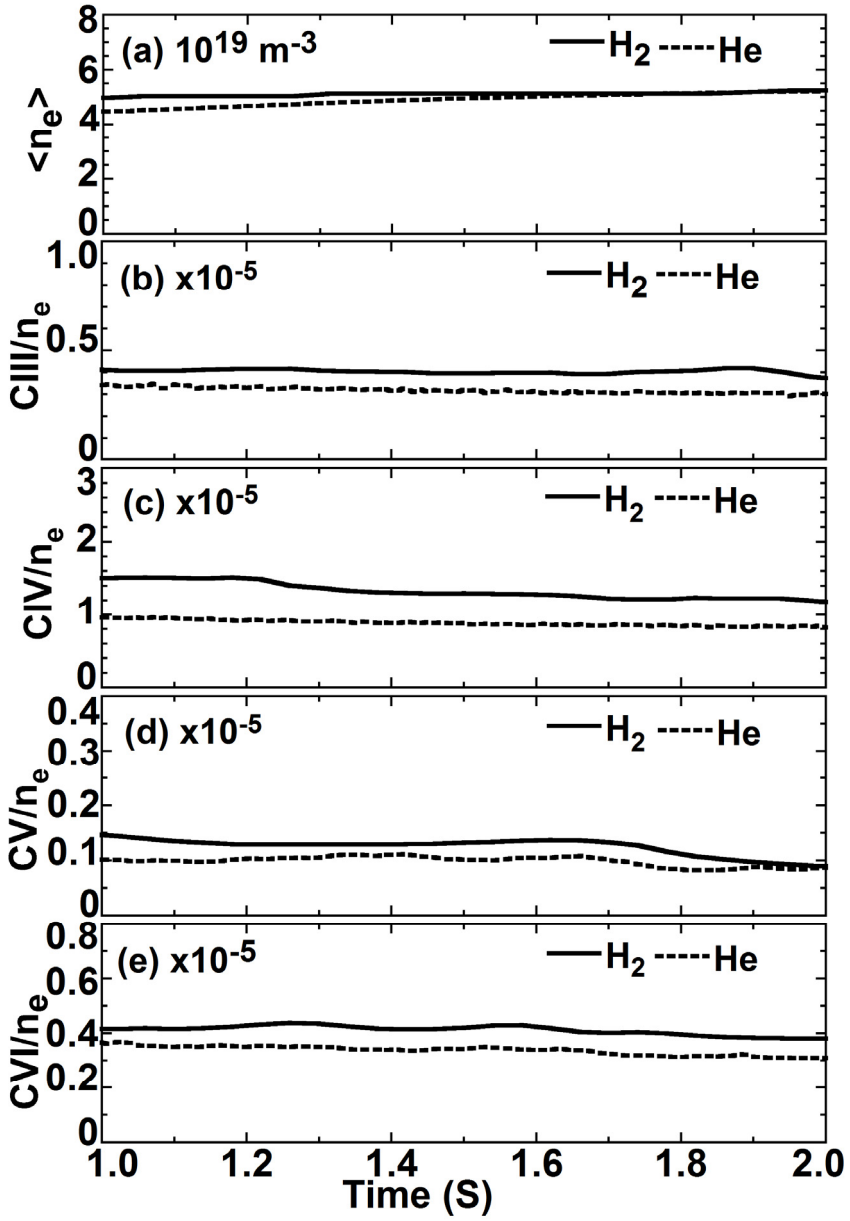

Fig.17. (a) Line-averaged density, $<n_e>$ and normalized intensities of (b) CIII/n_e, (c) CIV/n_e, (d) CV/n_e and (e) CVI/n_e in H_2 (solid lines) and He (dashed lines) discharges. Unit for carbon emissions of CIII (977Å), CIV (1548Å), CV (40.27Å) and CVI (33.73Å) is in 10^{14} photons.cm^{-2}.sr^{-1}.s^{-1}/10^{19}m^{-3}.

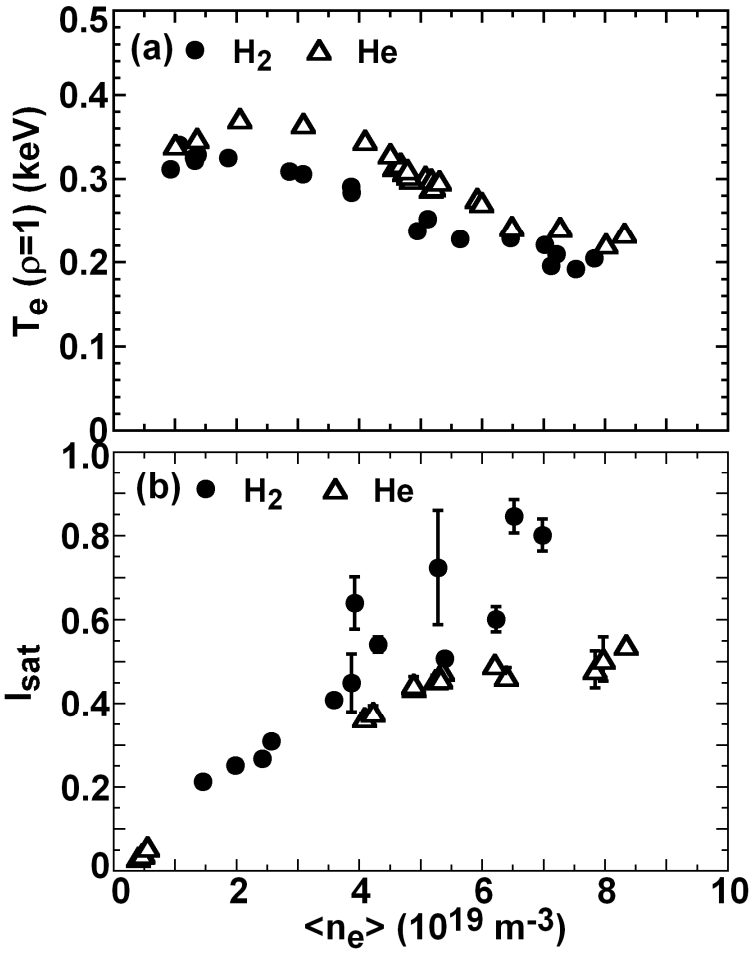

Fig.18. (a) T_e at ρ=1 and (b) divertor ion saturation current, I_{sat}, as a function of $\langle n_e \rangle$ for H_2 (closed circles) and He (open triangles) discharges.

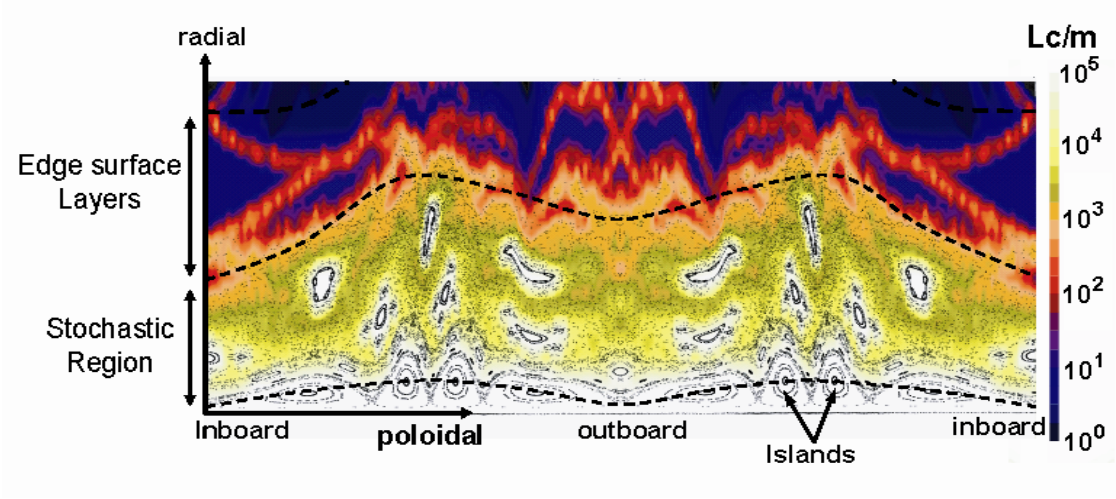

Fig.19. Two-dimensional connection length, L_c, profile in ergodic layer of LHD (R_{ax}=3.75m) superposed with Poincare plot of magnetic field lines.

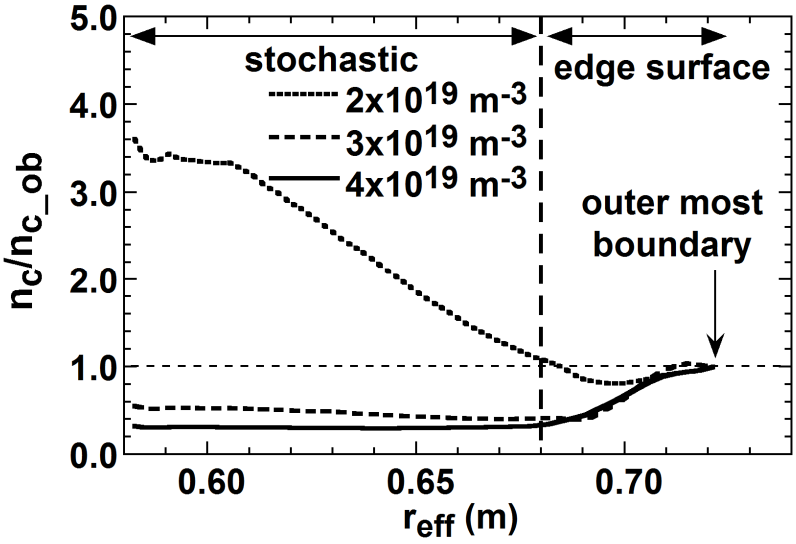

Fig.20. Edge profiles of carbon density summed up over all charge states for different densities: (a) $n_{LCFS}=2\times10^{19}m^{-3}$ (dotted line), $3\times10^{19}m^{-3}$ (dashed line) and $4\times10^{19}m^{-3}$ (solid line). $n_c/n_{c\text{-}ob}$ is carbon density normalized to total carbon density at outermost boundary of ergodic layer. Horizontal axis represents minor radius r_{eff} which is defined by cylindrical approximation. Vertical dashed line indicates the boundary between stochastic region and edge surface layers as shown in Fig.19.

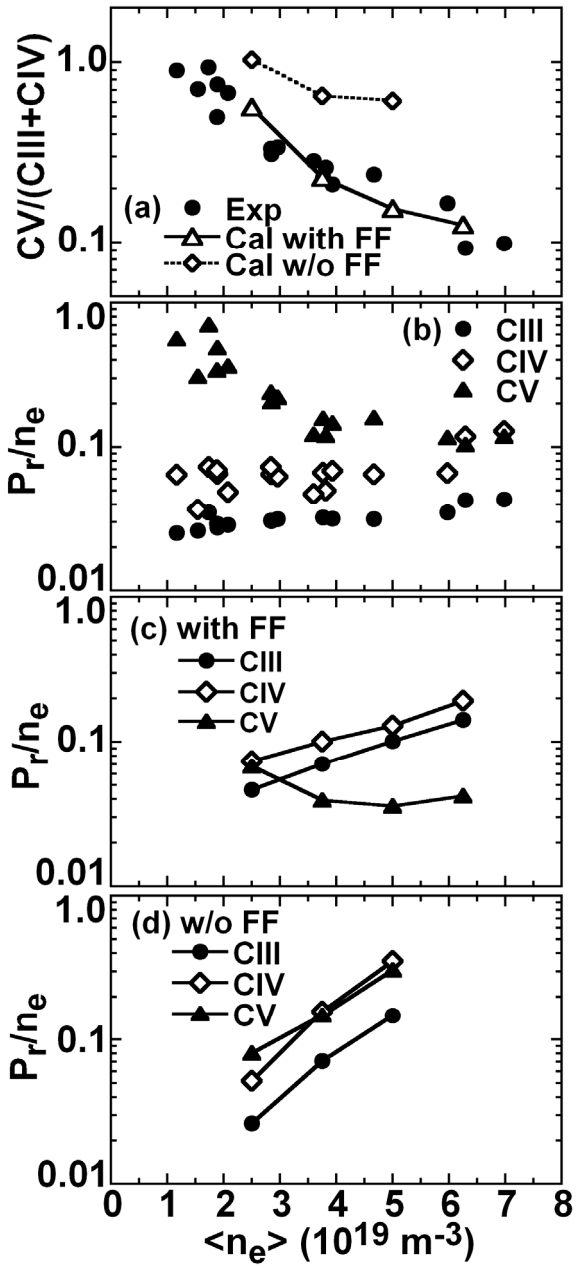

Fig.21. (a) Ratios of CV to CIII+CIV from experiment (closed circles) and simulation with (open triangles+solid line) and without (open diamonds+dotted line) friction force as a function of $<n_e>$ and normalized line radiations of CIII/n_e (closed circles), CIV/n_e (open diamonds) and CV/n_e (closed triangles) from (b) experiment and simulations (c) with and (d) without friction force in unit of kW/$10^{19}$$m^{-3}$ as a function of $<n_e>$. Ratios from simulation are normalized to experimental value of $3.7\times10^{19}$$m^{-3}$.

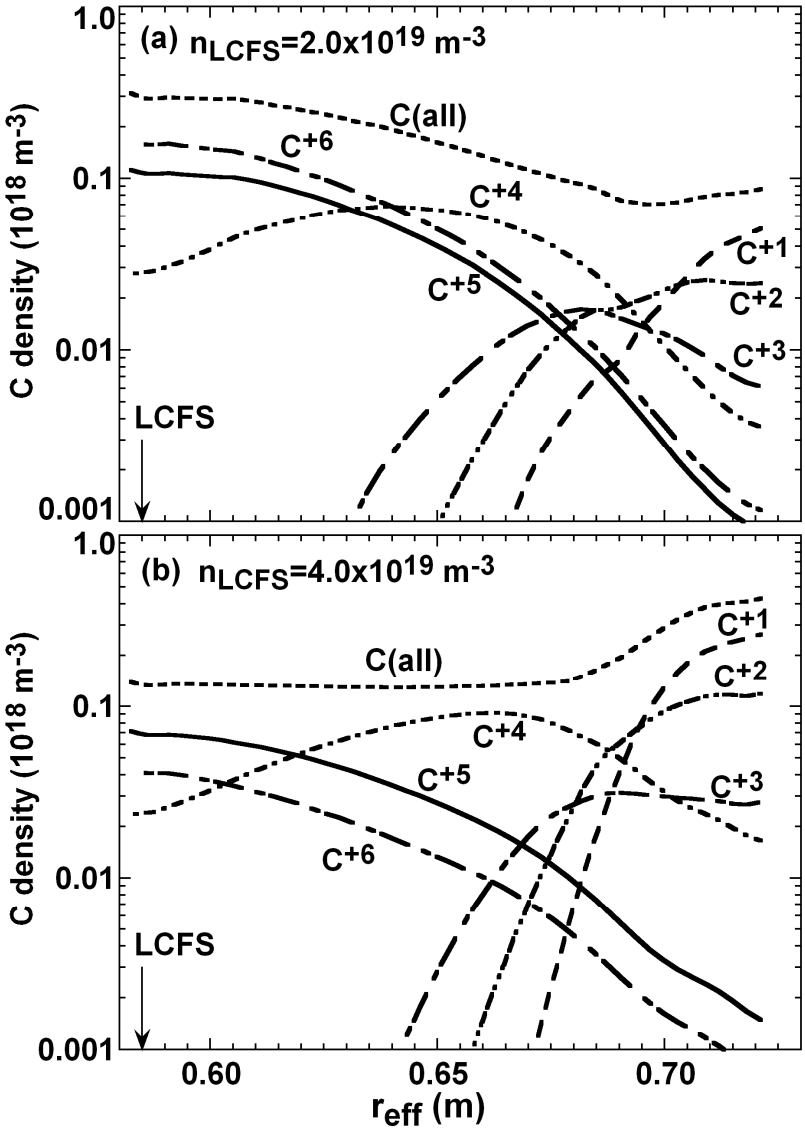

Fig.22. Radial carbon density profiles of each charge state simulated by EMC3-EIRENE code with (a) $n_{LCFS}=2\times10^{19}$ and (b) 4×10^{19}m^{-3}. Solid vertical arrows indicate position of LCFS for R_{ax}=3.75m.